AUTOMATED CELLULAR ELECTROPHYSIOLOGY TO INVESTIGATE THE ROLE OF INTERNEURONS IN ALZHEIMER'S DISEASE

A Dissertation
Presented to
The Academic Faculty

By

Mercedes Gonzalez

In Partial Fulfillment
of the Requirements for the Degree
Doctor of Philosophy in the
George W. Woodruff School of Mechanical Engineering
Department of Mechanical Engineering

Georgia Institute of Technology

August 2024

AUTOMATED CELLULAR ELECTROPHYSIOLOGY TO INVESTIGATE THE ROLE OF INTERNEURONS IN ALZHEIMER'S DISEASE

Thesis committee:

Co-advisor:
Dr. Craig Forest
Department of Mechanical Engineering
Georgia Institute of Technology

Co-advisor:
Dr. Matthew Rowan
Department of Biological Sciences
Emory University

Dr. Annabelle Singer
Department of Biomedical Engineering
Georgia Institute of Technology

Dr. Bilal Haider
Department of Biomedical Engineering
Georgia Institute of Technology

Dr. Christopher Rozell
Department of Electrical & Computer Engineering
Georgia Institute of Technology

Date approved: April 24, 2024

Just keep swimming.

Dory

For Mike and the M-Cats.

ACKNOWLEDGMENTS

I would like to start by thanking my advisors. To Craig Forest, thank you for believing in me for these 5 years and for mentoring me, both in research and in life. Thank you for making PBL such a wonderful place to work and for curating a group of wonderful scientists that I will have as lifelong friends. To Matthew Rowan, thank you for guiding me into the world of neuroscience and spending countless hours with me at the rig when I first started. I cannot imagine where I would be today without both of you. And thank you to my committee, Annabelle Singer, Bilal Haider, and Chris Rozell, for helping shape my experiments and strengthening my thesis.

I would like to thank the current members of PBL: Athena Chien, Ben Magondu, Sam Ehrlich, Ally Dunnum, and Bo Yang. Thank you for supporting and encouraging me this past year or so, both when I had great success and great failure in my experiments. Thank you to the PBL alumni that I was lucky enough to work with: Corey Landry, Colby Lewallen, Mighten Yip, Phoebe Welch, and Nina Sara Fraticelli-Guzman. I will forever be grateful for the technical and emotional support that you all provided, without which my PhD would have been impossibly difficult. Thank you to my BioE Mentor, Dan Zhang, who has shown me what it means to be a true friend and leader. And thank you to my BioE Mentee, Erin Shappell, who has been such a source of light and positivity during my time at Georgia Tech.

Thank you to my undergraduate research advisors, Douglas Bristow and Robert Landers, and the members of the Incremental Sheet Forming lab, who inspired me to even consider graduate school. Thank you for giving me the research experiences, confidence, and empowerment to do something I never imagined I could do.

Thank you to my mom and dad, Pam and Frank Gonzalez, who have unconditionally supported me through my 22 years of school. Thank you for all of the sacrifices you made to make my college experience possible and thank you for your love each and every day.

Thank you to my sister, Marissa, who has shown me what real hard work means and who inspires me everyday.

Thank you to my cats, Mu and Miso, for making every non-research moment a happier one. And last, but certainly not least, thank you to my husband, Mike Rouleau, who has been with me through each step of this PhD. Thank you for encouraging me to apply to Georgia Tech, even though I did not think I would get in. Thank you for listening to every complaint and for celebrating every victory I have had since day one. And thank you for always assuring me that I really can do this PhD.

TABLE OF CONTENTS

LIST OF TABLES

LIST OF FIGURES

LIST OF ACRONYMS

Aβ Amyloid Beta

AAV adeno-associated virus

ACC anterior cingulate cortex

aCSF artificial cerebrospinal fluid

AD Alzheimer's disease

App^{SAA} human amyloid precursor protein knock in model

CNN convolutional neural network

CSF cerebrospinal fluid

EC entorhinal cortex

EEG electroencephalography

GABA gamma-aminobutyric acid

GFP green fluorescent protein

IL infralimbic

LFP local field potential

M2 secondary motor cortex

MEG magnetoencephalography

mPFC medial prefrontal cortex

MRI magnetic resonance imaging

NFT neurofibrillary tangles

PET positron emission tomography

PL prelimbic

PV parvalbumin

V1 primary visual cortex

SUMMARY

Alzheimer's disease (AD) is a progressive neurodegenerative disease, accounting for about two thirds of dementia cases. Despite significant efforts to diagnose and cure AD, there are still no effective therapeutics to halt disease progression. While the conventional understanding attributes memory loss to the buildup of amyloid and tau proteins, emerging evidence suggests that cognitive decline in AD may stem from neuronal circuit dysregulation rather than protein aggregation. Specifically, alterations in the excitability of inhibitory interneurons may contribute to circuit dysfunction, although the evolution of this dysregulation across brain regions and over time remains poorly understood. To address this gap, the goal is to systematically investigate the emergence of parvalbumin (PV) interneuron dysfunction in AD, hypothesizing their early involvement in vulnerable brain regions.

In order to study these PV interneurons at the single cell level, with sufficient spatial and temporal resolution, this thesis will utilize patch clamp electrophysiology. The patch clamp technique is remains necessary for fully elucidating cell-type-specific behavior, although it is difficult and time-intensive. While patch clamp systems have emerged that automate certain aspects of the procedure, there remain challenges that can be remedied with improved automation techniques. To overcome these obstacles, several strategies have been developed to improve the success rates and facilitate the execution of automated, high-throughput investigations. In the initial identification of cells within acute brain slices, a deep learning methodology automatically nominates neurons for subsequent automated experiments. Addressing concerns regarding pipette localization errors, a convolutional neural network (CNN), specifically ResNet101, has been adapted and trained to autonomously detect and rectify the misplacement of pipette tips during automated *in vitro* patch clamp experiments. Furthermore, to facilitate investigations into synaptic connections between neurons, a method named patch-walking was demonstrated in brain slices, enabling efficient finding of synaptic connections.

CHAPTER 1
INTRODUCTION AND BACKGROUND

1.1 Studying the brain

Studying the brain is not only fascinating due to its incredible complexity but also crucial for unlocking the mysteries of human cognition and behavior. As the most intricate organ in the human body with over 100 billion neurons, the brain orchestrates a multitude of functions, from sensory perception to higher-order cognitive processes like memory, decision-making, and creativity [1]. Its complexity lies not only in its sheer number of cells and simultaneous computations, but also in its dynamic and adaptable nature, capable of learning, plasticity, and self-regulation [2]. The brain serves as the command center for all physiological and psychological processes, governing everything from basic motor functions to complex thought processes and emotions [2] (Figure 1.1). By studying the brain, researchers can decipher how neural circuits process information, form memories, generate behaviors, and adapt to environmental changes. Such insights not only deepen our understanding of human nature but also hold the key to developing effective treatments for neurological and psychiatric disorders, improving mental health outcomes, and enhancing overall well-being.

The basic neuroanatomy of the brain provides a structural framework for understanding how different regions contribute to various functions, yet the intricate workings of these regions are not fully understood. The brain is organized into distinct regions, each with specialized roles in processing sensory information, regulating emotions, controlling movement, and governing higher cognitive functions [3, 2]. For instance, the frontal lobe is involved in decision-making and executive control, the temporal lobe in memory formation and auditory processing, and the occipital lobe in visual perception [4]. Additionally, sub-

cortical structures such as the hippocampus and basal ganglia play critical roles in learning, memory, and motor control [2, 5]. The precise mechanisms underlying how these regions interact and coordinate to produce complex behaviors and cognitive processes are still not fully understood [3]. There are numerous approaches for investigating how the brain generates complex behaviors, spanning from examining the macroscale through techniques like electroencephalography (EEG), magnetoencephalography (MEG), and magnetic resonance imaging (MRI), to the mesoscale using tools such as local field potential (LFP) electrodes, and, crucially, analyzing the individual building blocks of the brain: neurons.

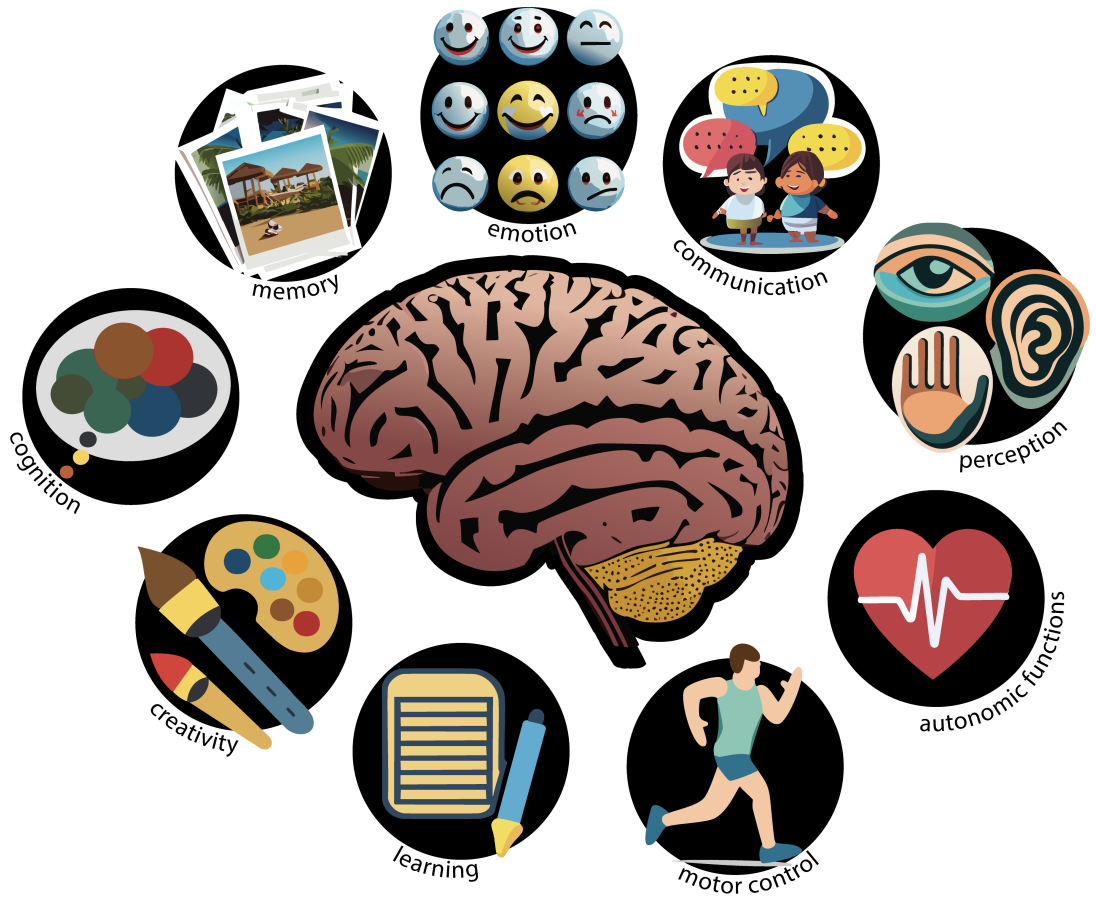

Figure 1.1: Graphical representation of the brain and its role in our lives: from complex thought processes such as cognition and emotion to autonomic functions and motor control.

Neurons are the fundamental units composing the intricate architecture of the brain, serving as the basic building blocks of neural networks. These specialized cells possess

unique structures and functions crucial for information processing within the nervous system. Structurally, a typical neuron consists of a soma (cell body), dendrites, and an axon covered in myelin sheath, as shown in Figure 1.2A. Dendrites receive signals from other neurons or sensory receptors, while the axon transmits electrical impulses, known as action potentials, to other neurons. The membrane consists of a lipid bilayer embedded with ion channels, which regulate the concentrations of ions such as Na+, K+, and Cl- in the cell as shown in Figure 1.2B, influencing the neuron's electrical characteristics. The movement of ions across the membrane leads to fluctuations in its potential. Typically, a neuron maintains a resting membrane potential of around -60 to -70 mV. Once this potential reaches a threshold, the neuron initiates an action potential, as shown in Figure 1.2C. This occurs due to an influx of Na+ ions into the cell, causing depolarization. Subsequently, as sodium channels close, potassium channels open, allowing K+ ions to exit the cell and repolarize it. Following a recovery period, the cell returns to its resting state.

The communication between neurons primarily occurs at specialized junctions called synapses, as highlighted in Figure 1.2B. When an action potential reaches the presynaptic terminal of one neuron, it triggers the release of neurotransmitters into the synaptic cleft, which then bind to receptors on the postsynaptic membrane of the receiving neuron, leading to the generation of new electrical signals. This process enables neurons to transmit information across neural circuits, forming the basis of complex cognitive functions and behaviors.

Studying the brain has immense implications for advancing medical treatments, particularly in the realm of neurological and psychiatric disorders. Neurodegenerative diseases such as Alzheimer's, Parkinson's, and Huntington's disease pose significant challenges due to their complex etiology and lack of effective therapies [8]. By elucidating the underlying mechanisms of these diseases, researchers can identify novel therapeutic targets and develop innovative treatment strategies aimed at halting disease progression, mitigating symptoms, and improving patient outcomes.

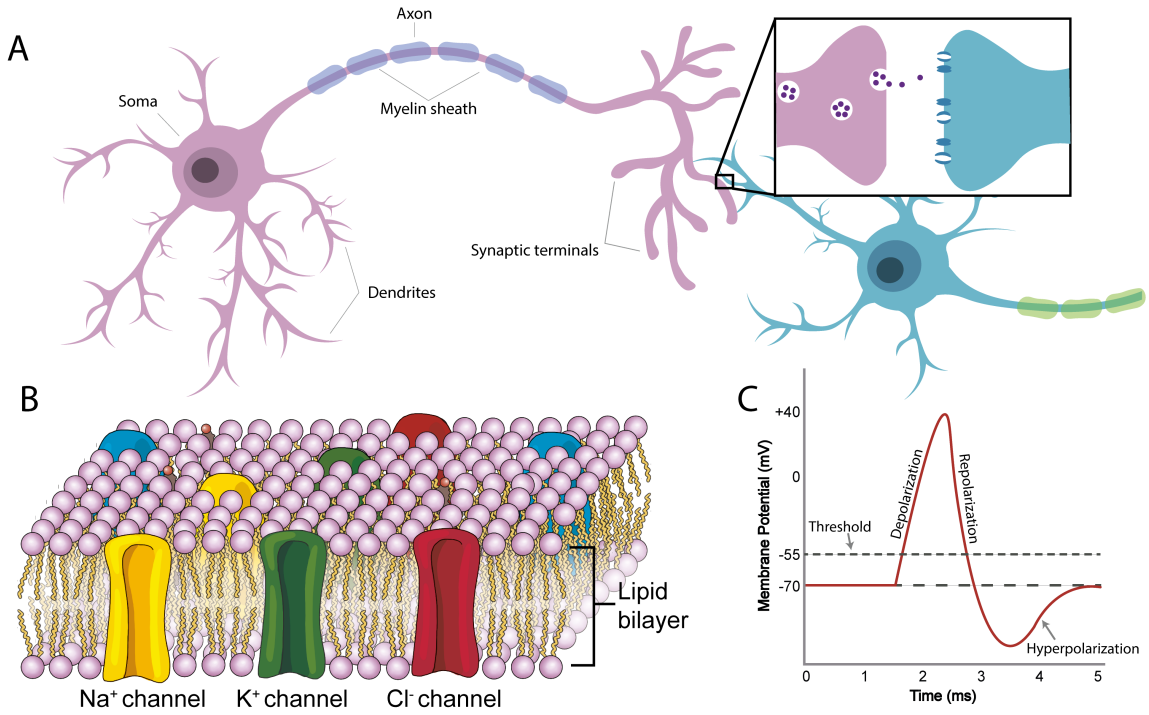

Figure 1.2: A. Graphical representation of the human brain, highlighting the granularity of neurons in the brain. [6] B. Cartoon schematic of a neuron, with a close-up of a synaptic cleft. C. Close up view of a neuron's membrane, displaying the lipid bilayer and representative ion channels. D. Diagram of an action potential, with indicators on the threshold, depolarization, repolarization, and hyperpolarization. (Adapted from [7].)

1.2 Alzheimer's disease

1.2.1 Definition and Impact

AD stands as a formidable neurodegenerative disorder characterized by progressive cognitive decline and memory impairment. Its pathological hallmarks include the accumulation of amyloid-beta plaques and tau protein tangles in the brain, leading to synaptic dysfunction, neuronal loss, and ultimately, cognitive impairment [9, 10, 11] (Figure 1.3A). AD typically manifests with mild onset symptoms and gradually worsens over time, significantly impacting affected individuals' daily functioning and quality of life. While memory loss represents a prominent early symptom, AD eventually affects multiple cognitive domains, including language, executive function, and visuospatial abilities [11]. As the most

common cause of dementia, AD poses significant challenges for healthcare systems and societies worldwide [12], necessitating urgent attention and innovative approaches to diagnosis, treatment, and care.

The prevalence of AD has reached epidemic proportions, affecting tens of millions of individuals worldwide and posing a substantial burden on global healthcare systems [13]. Currently, AD accounts for the majority of dementia cases, making it the leading cause of cognitive impairment among older adults [14]. With an aging population and increasing life expectancy, the prevalence of AD is expected to escalate dramatically in the coming decades, placing further strain on healthcare resources and caregiver support networks [13]. Beyond the individual suffering experienced by those diagnosed with AD, the disease exerts profound emotional, financial, and societal tolls on families and communities. Addressing the global impact of AD requires concerted efforts to raise awareness, improve early detection and diagnosis, and develop effective interventions aimed at mitigating disease progression and enhancing the quality of life for affected individuals and their caregivers.

1.2.2 Hallmarks and Therapeutic Approaches

The hallmarks of AD in humans encompass a spectrum of pathological changes that contribute to cognitive decline and neurodegeneration. Amyloid Beta (Aβ) plaques and tau protein tangles represent the classic neuropathological features observed in AD brains [18]. Aβ plaques, formed by the aggregation of amyloid-beta peptides, disrupt synaptic function and trigger neuroinflammation, contributing to neuronal dysfunction and loss [19] (Figure 1.3B). Tau protein abnormalities, characterized by hyperphosphorylation and aggregation into neurofibrillary tangles, disrupt intracellular transport and cellular integrity, further exacerbating neuronal damage [19]. Understanding the complex interplay of these pathological changes is crucial for elucidating the mechanisms underlying AD pathogenesis and developing targeted therapeutic interventions.

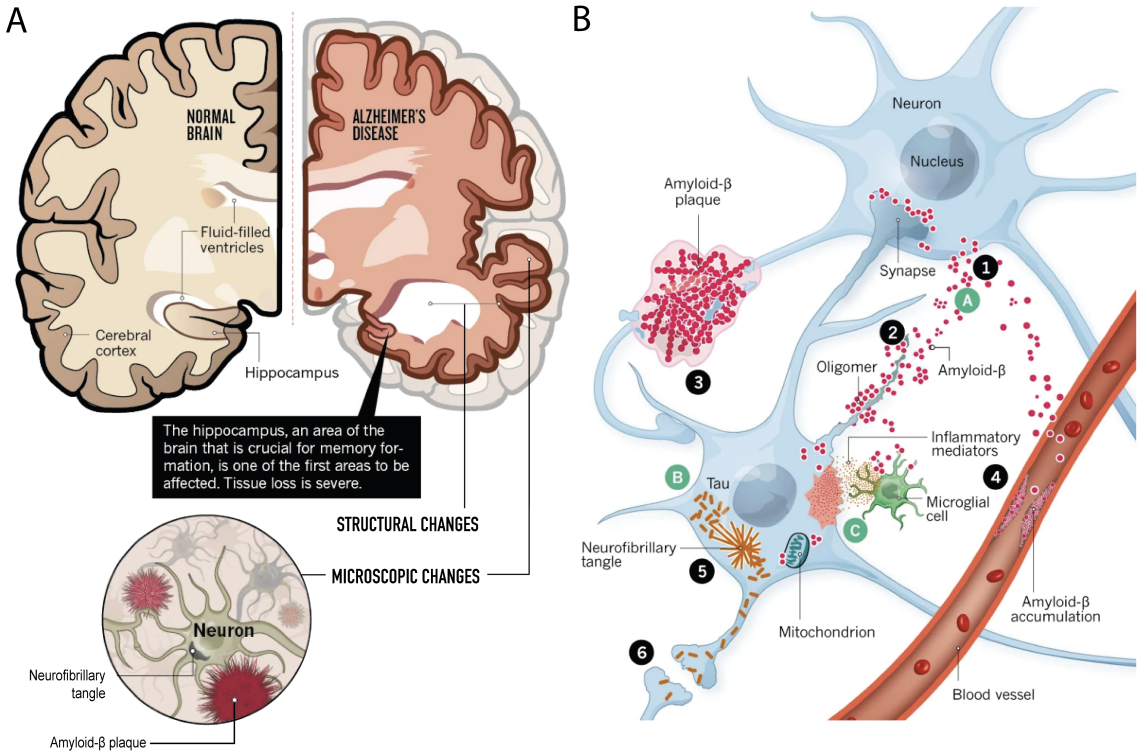

Figure 1.3: A. Graphical representation of Alzheimer's disease hallmarks. B. Amyloid beta and tau and their role in Alzheimer's disease. [15, 16, 17]

Genetic factors play a significant role in AD susceptibility and progression. Mutations in genes such as APP, PSEN1, and PSEN2 are associated with familial forms of AD, accounting for a small percentage of cases [20]. Additionally, common genetic variants, such as those in the APOE gene, influence the risk and age of onset of sporadic AD [21]. These genetic insights have informed our understanding of AD pathophysiology and provided targets for therapeutic intervention. Various therapeutic approaches have been explored, targeting different aspects of AD pathology, including Aβ production, tau aggregation, neuroinflammation, and synaptic dysfunction [22]. However, despite extensive research efforts, the development of disease-modifying therapies remains elusive, highlighting the need for continued exploration of novel treatment strategies and personalized approaches based on genetic risk factors.

1.2.3 Challenges in Diagnosis

Diagnosing AD poses significant challenges due to its heterogeneous clinical presentation and overlapping symptoms with other forms of dementia. Currently, diagnosis relies primarily on clinical evaluation, neuropsychological testing, and biomarker assessments [23]. Biomarkers, including cerebrospinal fluid (CSF) levels of Aβ and tau proteins, amyloid positron emission tomography (PET) imaging, and hippocampal volume on MRI, aid in the detection of AD pathology and differential diagnosis from other dementias [24, 25]. However, these biomarkers are not universally accessible, and their interpretation requires expertise, limiting their widespread clinical utility. Furthermore, accurate diagnosis at early disease stages remains particularly challenging, as symptoms may be subtle and nonspecific [26, 27]. Addressing these diagnostic challenges requires the development of more sensitive and specific biomarkers, as well as innovative diagnostic tools and approaches that enable early detection and intervention, ultimately improving patient outcomes and management of AD.

1.2.4 Mouse Models

To more efficiently study AD, mouse models serve as valuable tools for investigating the pathophysiology of the disease and evaluating potential therapeutic interventions. These models encompass a diverse array of genetic, transgenic, and knock-in mouse lines engineered to recapitulate key aspects of AD pathology, including Aβ accumulation, tau hyperphosphorylation, and neuroinflammation as shown in Figure 1.4. Commonly used AD mouse models include the APP/PS1, 5xFAD, and APP/PS1/tau triple transgenic mice, each exhibiting specific features of AD pathology [28].

1.2.5 Prevailing Hypothesis: Amyloid-Beta and Tau

The prevailing hypothesis in AD research has long focused on the role of Aβ and tau proteins in disease pathogenesis. According to this hypothesis, the accumulation of Aβ pep-

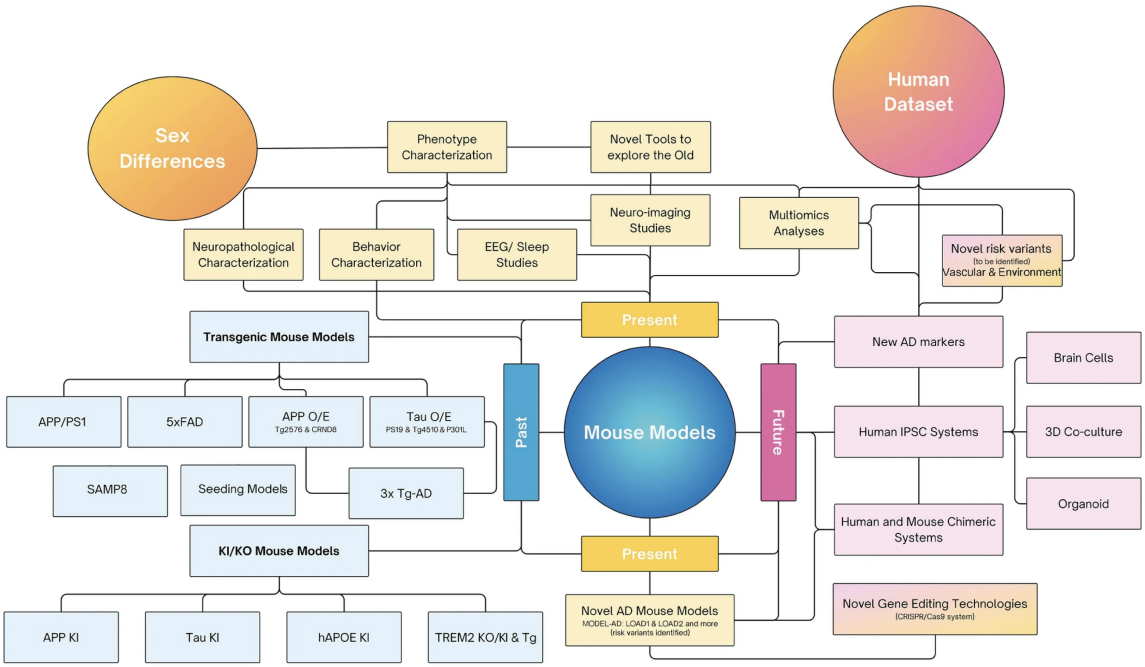

Figure 1.4: Flow chart summarizing the past, present, and future of Alzheimer's disease models and technical approaches [28]

tides into plaques and the hyperphosphorylation of tau proteins into neurofibrillary tangles disrupt neuronal function and lead to synaptic dysfunction, neuroinflammation, and ultimately neurodegeneration [29, 30, 31]. This hypothesis has guided much of the research and therapeutic development efforts in the field, with numerous clinical trials targeting Aβ and tau pathology [32]. However, despite considerable investment and advancements in understanding AD pathophysiology, therapies targeting Aβ and tau have yet to demonstrate significant clinical efficacy, prompting a re-evaluation of the amyloid cascade hypothesis and the exploration of alternative mechanisms underlying AD pathogenesis.

1.2.6 Emerging Perspectives: Circuit Hyperexcitability

Emerging evidence suggests that circuit hyperexcitability may represent an early and critical event in AD pathogenesis [34, 35, 36]. Studies using animal models have revealed aberrant neuronal activity and network synchronization preceding the onset of classic pathological hallmarks such as Aβ plaques and tau tangles [37, 38, 39, 40, 41]. Circuit hy-

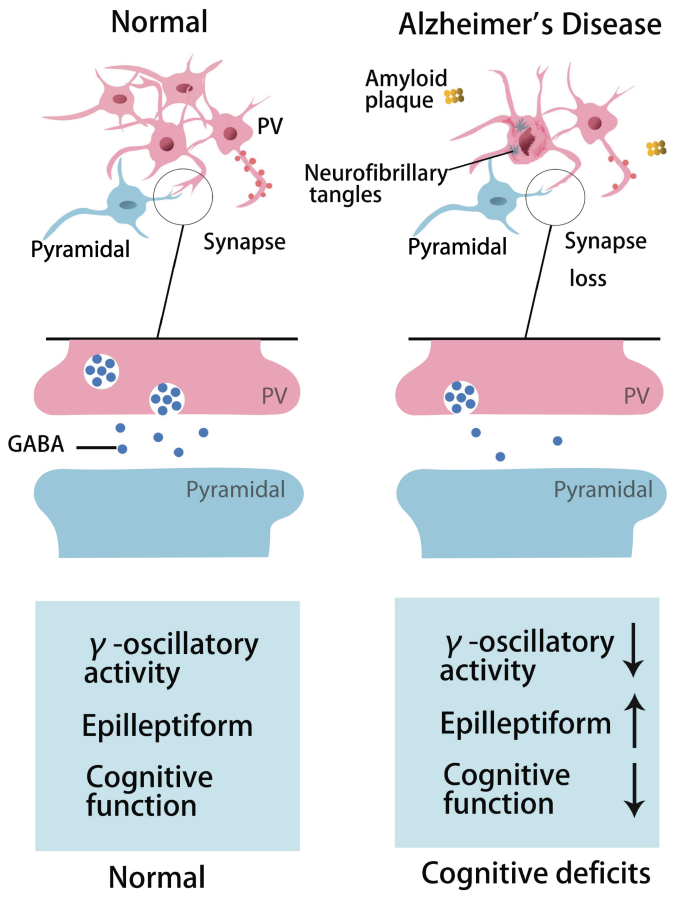

Figure 1.5: Hypothesized relationship between PV interneurons and pyramidal cells in normal brains (left) and in Alzheimer's disease (right) [33]

perexcitability is thought to result from disruptions in the balance between excitatory and inhibitory neurotransmission, leading to network instability, synaptic dysfunction, and cognitive impairment [42]. While the precise mechanisms underlying circuit hyperexcitability in AD remain incompletely understood [43, 44], dysregulation of ion channels, neurotransmitter systems, and interneuron dysfunction have been implicated. Dysregulation of voltage-gated sodium and calcium channels, for instance, disrupts neuronal excitability and contributes to aberrant network activity [44]. Changes in neurotransmitter systems, including glutamate and gamma-aminobutyric acid (GABA), further disrupt excitatory-inhibitory balance, leading to network hyperactivity [33]. Additionally, alterations in interneuron function, particularly PV interneurons, impair local circuit inhibition and exacerbate net-

work hyperexcitability[45, 46]. Neuroinflammation, oxidative stress, and mitochondrial dysfunction also contribute to neuronal hyperexcitability and exacerbate neurodegeneration in AD [47]. Understanding the multifactorial nature of hyperexcitability in AD is essential for developing targeted therapeutic interventions aimed at restoring neural circuit homeostasis and mitigating cognitive decline.

1.2.7 Parvalbumin Interneurons

PV interneurons play a crucial role in maintaining the balance and stability of healthy brain circuits[48]. As a subtype of inhibitory interneurons, PV interneurons regulate neural activity by providing precise and rapid inhibition to excitatory neurons within local microcircuits. Through their fast-spiking properties and synchronous firing patterns, PV interneurons contribute to the generation of gamma oscillations and the synchronization of neuronal ensembles during cognitive tasks such as sensory processing, attention, and memory formation [49]. By modulating the timing and synchrony of neuronal firing, PV interneurons sculpt the activity patterns of neuronal networks, ensuring efficient information processing and preventing the emergence of pathological states such as epileptic seizures [50]. Thus, PV interneurons are indispensable components of healthy brain function, exerting tight control over circuit dynamics and supporting cognitive processes.

The dysfunction of PV interneurons may contribute to cognitive impairment and disease progression [51, 52, 53, 54]. Studies using animal models have revealed alterations in the firing of PV interneurons in AD [51, 55, 56, 57, 58, 59]. Dysregulation of PV interneurons likely disrupts inhibitory control within local circuits, leading to circuit hyperexcitability, synaptic dysfunction, and cognitive deficits characteristic of AD (Figure 1.5). Furthermore, PV interneuron dysfunction may exacerbate amyloid-beta and tau pathology, contributing to neurodegeneration and disease progression[60, 61, 62]. Understanding the role of PV interneurons in AD pathophysiology may provide insights into the mechanisms underlying cognitive decline and inform the development of targeted therapeutic strategies aimed at

restoring inhibitory function and preserving neural circuit integrity.

To effectively investigate the role of these PV interneurons in AD, a high resolution, cell-type specific approach should be taken. One of the most powerful techniques used to study the electrical properties of individual cells, particularly neurons, with unparalleled precision, is patch clamp electrophysiology.

1.3 Patch clamp electrophysiology

The patch clamp method involves placing a glass micropipette, or patch pipette, onto the cell membrane to form a tight seal, allowing for the measurement of ion currents and voltage changes across the membrane. Patch clamp recordings can be performed in different configurations, including whole-cell, cell-attached, inside-out, and outside-out, each offering unique insights into cellular function [63]. This technique enables researchers to investigate various aspects of neuronal physiology, such as action potential firing, synaptic transmission, ion channel kinetics, and membrane potential dynamics [2]. Patch clamp electrophysiology has broad applications in neuroscience, ranging from basic research on neuronal excitability and synaptic plasticity to drug discovery and screening for neurological disorders [64, 65, 66, 67]. By providing direct measurements of cellular electrical activity, patch clamp recordings offer invaluable insights into the fundamental mechanisms underlying neuronal function and dysfunction in health and disease.

The manual patch clamp technique remains a cornerstone method in neuroscience research due to its unparalleled ability to provide high-fidelity recordings of neuronal activity. One of its primary advantages is its exceptional sensitivity, allowing for the precise measurement of ion channel currents and membrane potentials at the single-cell level [68]. This level of detail enables researchers to characterize ion channel kinetics, synaptic transmission properties, and intrinsic neuronal properties with remarkable accuracy. Additionally, the manual patch clamp technique offers flexibility in experimental design, allowing for the investigation of various cell types, neuronal compartments, and experimental condi-

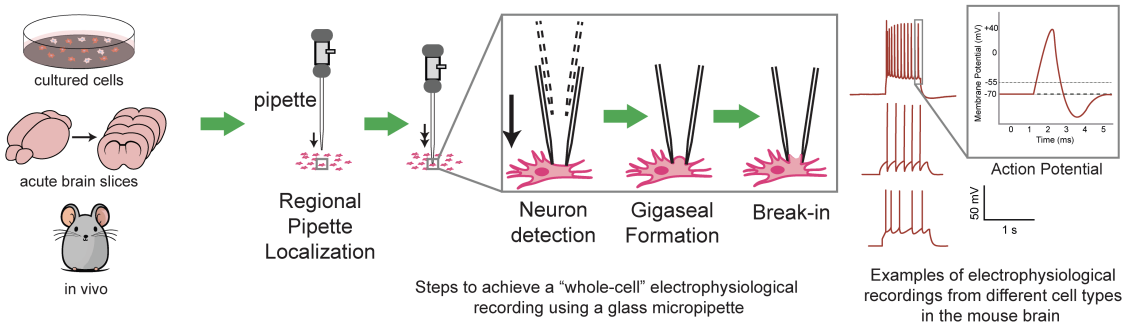

Figure 1.6: Schematic demonstrating the steps of the patch clamp technique: (1) prepare sample, either cultured cells, acute brain slices, or *in vivo* mice, (2) localize the pipette, (3) neuron detection, (4) gigaseal formation, (5) break-in to acheive whole cell configuration.

tions (Figure 1.6). Despite these advantages, manual patch clamp recordings are labor-intensive and time-consuming, requiring skilled operators and meticulous technique [69]. The method also suffers from low throughput, limiting its applicability for large-scale studies and screening applications. Furthermore, manual patch clamp recordings are susceptible to operator bias and variability, necessitating rigorous quality control measures to ensure data reliability and reproducibility. Overall, while the manual patch clamp technique remains the gold standard for electrophysiological recordings, its limitations underscore the need for continued innovation and development of automated patch clamp technologies to address scalability and throughput challenges in neuroscience research [70].

To improve the throughput and yield of these essential yet challenging experiments, several groups have invented automated patch clamp rigs for both *in vitro* [71, 72, 73] and *in vivo* [74, 75, 76, 77, 78, 79] electrophysiology, including a handful of techniques developed specifically for automated pipette localization [80, 81, 82] and cell tracking [83]. The adoption of automatic patch clamp technology has facilitated large-scale studies, drug screening assays, and high-throughput screening campaigns, accelerating the pace of discovery in neurobiology and drug development [70]. Despite the significant advancements in automatic patch clamp technology, several challenges and gaps in automation persist, hindering its widespread adoption and application in neuroscience research. Addressing these challenges will require ongoing technological innovation, optimization of experimen-

tal protocols, and collaboration between researchers and instrument developers to enhance the performance and capabilities of automatic patch clamp platforms.

1.4 Experimental Approach

The application of patch clamp electrophysiology in studying PV interneurons in AD models offers a unique opportunity to elucidate the cellular mechanisms underlying circuit dysfunction and cognitive impairment. Given the emerging evidence implicating PV interneuron dysfunction in AD pathophysiology, patch clamp recordings provide a direct means to investigate alterations in the excitability, synaptic connectivity, and firing properties of PV interneurons in AD-related brain regions. The approach involves acute brain slice preparations from AD mouse models, followed by targeted patch clamp recordings from PV interneurons and nearby excitatory neurons in regions such as the entorhinal cortex, visual and motor cortices, and prefrontal cortex.

The hypothesis driving this work predicts that PV interneurons are hypoexcitable in brain regions that are implicated in early AD, but not across the entire cortex. Furthermore, in regions where there is hypoexcitability of inhibitory cells, there is likely hyperexcitability of excitatory neurons, as a result of reduced inhibition. By characterizing the intrinsic properties of PV interneurons and excitatory cells with patch clamp electrophysiology, this thesis will systematically address four major brain regions in an AD mouse model. Insights gained from patch clamp recordings may reveal altered excitability, potentially uncovering novel therapeutic targets for restoring neural circuit function and mitigating cognitive deficits.

CHAPTER 2

MACHINE LEARNING-BASED PIPETTE POSITIONAL CORRECTION FOR AUTOMATIC PATCH CLAMP *IN VITRO*

2.1 Introduction

Characterizing neuronal function on a single cell level is crucial to unraveling the biological mechanisms underlying brain activity. One of the most important techniques used in neuroscience to understand individual neuron behavior is patch clamp electrophysiology. This Nobel prize-winning technique allows one to record sub-threshold current and voltage changes, enabling scientists to better understand neuronal communication. While optical methods offer a promising non-invasive method to study single neurons [84, 85, 86, 87], their reliance on relative measurements rather than absolute voltage or current and sub-optimal spatiotemporal resolution still require patch clamp to validate recordings of individual cellular behavior.

Typically, an *in vitro* patch clamp experiment is performed as follows: one views a brain slice under a microscope, manually maneuvers and delicately places a 1-2 μm tip of a glass pipette into contact with a 10 μm diameter cell membrane, creates a high-resistance seal between the pipette and cell membrane, and breaks into the cell to create a whole-cell configuration. This technique is immensely time intensive even for a skilled expert under optimal conditions. To improve the throughput and yield of these essential yet challenging experiments, several groups have invented automated patch clamp rigs for both *in vitro* [71, 72, 73] and *in vivo* [74, 75, 76, 77, 78, 79] electrophysiology, including a handful of techniques developed specifically for automated pipette localization [80, 81, 82] and cell tracking [83].

One of the most challenging steps to automate in these rigs is the accurate and repeat-

able placement of the pipette tip close to the membrane of a cell [82]. Conventionally, patch pipettes are controlled by micromanipulators that have random and systematic errors on the order of 10 μm [72] when repeatedly moving to and from the same location. A major drawback for previous pipette tip localization techniques [81, 80, 82] is that the accuracy is significantly reduced when real-world background lighting variation and noise is introduced. Light scattering from the brain tissue induces significant noise in the image and renders these methods practically useless since they rely on a clear image of the pipette in acute slice experiments, despite their success in cultured cell experiments. To overcome this obstacle, we implemented a convolutional neural network (CNN), ResNet101, to automatically identify and correct the pipette tip localization error for automated *in vitro* patch clamp experiments. This method will not only improve the precise placement of the pipette near the cell membrane, but also reduce the time required to localize the pipette tip over a cell and therefore improve the overall throughput and efficiency of the automated patch clamp process.

2.2 Methods

2.2.1 Coordinate System and Definition of Errors

To accurately identify the pipette location for patch clamp experiments, we defined a coordinate system relative to the objective location so that the center of the field of view, with the pipette tip in focus, was considered the origin. Hereafter, the view of the brain slice under the microscope will be referred to as the XY-plane. The Z direction is defined by the vertical distance perpendicular to that plane, with z = 0 at the location where the pipette was perfectly in focus.

There were three types of positioning errors addressed, as shown in Fig. Figure 2.1a. When moving the pipette, the pipette is commanded to move to the desired position (white), typically coincident with the center of a cell $(x, y)_{cell}$ in automated patch clamp experiments. Due to random and systematic errors in the 3-axis manipulators, the true pipette po-

sition (blue) is not equal to the desired position, resulting in the true pipette error ($\vec{t_x}$,$\vec{t_y}$,$\vec{t_z}$). We can estimate the true position of the pipette with the CNN, resulting in the computed CNN position (red). This CNN position has CNN error vector ($\vec{c_x}$,$\vec{c_y}$,$\vec{c_z}$), defined by the difference between the true pipette position and the CNN position. Since we cannot determine the true pipette position during an automated patch clamp experiment, we must use the CNN position as a feedback signal. Thus we use the difference between the desired position and the CNN position, called the measured error ($\vec{m_x}$,$\vec{m_y}$,$\vec{m_z}$), to correct the pipette's position.

2.2.2 Image Collection

The image data sets used for training, validation, and testing in this work consisted of 1024x1280 8-bit raw images. We used a standard electrophysiology setup (SliceScope Pro 3000, Scientifica Ltd) with PatchStar micromanipulators at a 24°approach angle. We used a 40x objective (LUMPFLFL40XW/IR, NA 0.8, Olympus) and Rolera Bolt camera (QImaging), illuminated under DIC with an infrared light-emitting diode (Scientfica). The resulting field of view was 116 x 92 μm. All animal procedures were done in accordance with the US National Institutes of Health Guide for the Care and Use of Laboratory Animals and the Georgia Institute of Technology animal care committee's regulations.

2.2.3 Neural Network Training, Validation, and Testing Data

To construct a representative data set of pipette images, images of 3-5 MΩ (1-2 μm diameter tip) pipettes were collected over a plain background as well as with a brain slice. The motivation for this is to ensure that the network would be robust enough to identify pipettes in both scenarios, if necessary. The ground truth annotation process began by sending a pipette to a computer-generated randomized location in the XY-plane ($\pm$ 27 μm). The user manually annotated the location of the pipette tip, in pixels, and confirmed the pipette was in focus so that the pipette could be imaged at fixed intervals along the Z-axis at

this position in the XY-plane. The pipette would then automatically move down (only in the Z direction) with a constant step size to a random lower limit distance of up to 100 μm, collecting images at each step and recording the manually annotated XY location and prescribed Z location (based on step size) as an (X,Y,Z) coordinate in pixels. The step sizes were constant for each XY location, but randomized (within 5-20 μm) in between. Once at the lower limit distance, the pipette would return to the in-focus position (Z=0) at the same XY location. To ensure that the pipette tip location was accurate, the user would again manually annotate the tip, saving the (X,Y) coordinate in pixels, while in focus. The pipette would then step in the positive Z direction, collecting images and recording coordinates at each step until reaching an upper limit distance. A total of 6678 raw annotated images were captured for training, validation, and testing data sets. All training and testing data will be available at autopatcher.org.

2.2.4 Image Preprocessing

All images used for training and validation were preprocessed using contrast stretching [88] to improve the ability to identify the pipette tip. To accomplish this, we calculated the average $(\bar{x})$ and standard deviations (σ) of the pixel intensities of each image and mapped the original pixel values to the range defined by $(\bar{x} \pm 2\sigma)$ for each image individually. This mapping improved the contrast by reducing the range of pixel intensities, thereby making a smaller range of pixel intensities more. Any pixel intensity that was outside the range of [0,1] after mapping was set to 0 or 1 respectively. The images were then cropped to a square from the center and downsized to 224x224 for use with the CNN. These images were then transformed to artificially increase the training data set, making the network more robust to different orientations of the pipette. The images, and their corresponding pipette tip location annotations, were flipped horizontally, vertically, and both horizontally and vertically. These 3 augmentations resulted in a total training data set of 24747 images and a validation data set of 765 images. The test images underwent the same preprocessing, but

no augmentations, resulting in a total of 300 test images. All preprocessing and network training was done using MATLAB 2020a and all patch clamp experiments were done with MATLAB and LabVIEW programs.

2.2.5 Convolutional Neural Network Training

The pretrained network model, ResNet101, was used as the basis for this work. ResNet101 is a convolutional neural network, 101 layers deep, that is trained for classification problems. The residual network family is known for performing well in classification challenges because the depth of these CNNs lead to superior performance [89]. Here, we wanted to predict the (X,Y,Z) location of the pipette tip based on an image. To accomplish this, we replaced the final three layers of the ResNet101 architecture with a fully connected layer and a regression layer [90]. This allowed us to define the output as a continuous 3x1 vector, corresponding to the (X,Y,Z) location of the pipette tip.

The training options are summarized in Table Table 2.1. Of the optimizers available in the MATLAB Deep Learning Toolbox, the *rmsprop* (root mean square propagation) optimizer, or loss function, has reported the greatest accuracy [91]. The mini batch size should be a power of 2 and maximized for accuracy [92]. While computer RAM availability was limited during training, we determined a mini batch size of 16 was suitable for this application. The number of epochs was determined experimentally, aiming to minimize root mean squared error (RMSE) during training while maximizing number of epochs to ensure sufficient adjusting of the CNN's weights. It is convention to have a dynamic learning rate, so the learn rate schedule was set to *piecewise*, where the learn rate began at the initial learn rate and monotonically decreased by the learn rate drop factor after each drop period (in epochs) [93]. Bengio et al. recommended beginning with a large learning rate and reducing the rate if the training loss does not converge. After testing a few different initial learn rates and drop factors, we found a suitable learn rate schedule to follow. The validation frequency and patience were set to their default values as suggested by MAT-

LAB [94]. We used a Dell Precision 5540 (NVIDIA GeForce GTX 1080 GPU, Intel(R) Core(TM) i7-9850H CPU @ 2.60GHz, 32 GB RAM, Windows 10, 64-bit) to train, validate, and test the CNN. The validation data was shuffled with each epoch to prevent the CNN from over-fitting to the training and validation sets.

Table 2.1: Convolutional Neural Network Training Options

Training Option	Setting
Solver	rmsprop
Mini Batch Size	16
Max Epochs	60
Initial Learn Rate	1e-4
Learn Rate Schedule	piecewise
Learn Rate Drop Factor	0.09
Learn Rate Drop Period	10
Validation Frequency	50
Validation Patience	Inf
Execution Environment	gpu
Shuffle	every epoch

2.2.6 Convolutional Neural Network Testing

To evaluate the accuracy of the CNN pipette tip identification used with an iterative proportional feedback controller, we performed a series of experiments over acute brain slices. Specifically, a LabVIEW program randomized the initial pipette location in the field of view (within $\pm$27 μm in the XY plane and $\pm$ 6 μm in the Z direction). The range of training data in the Z direction was limited to 6 μm since pipette localization error both near the edges of the field of view and out of focus was not observed; thus, did not warrant the excess training data. The CNN used the current image to determine the position of the pipette tip. From that CNN position, the measured error vector was calculated from the origin (center of the field of view, in focus) and used to correct the pipette location back to the origin. The CNN-based pipette tip identification algorithm was run recursively for a predetermined number of iterations (1-4). To determine the true pipette error after iterative correction, the pipette tip was then manually moved to the origin and the change in the

manipulator position was saved as the true pipette error.

2.2.7 Patch Clamp Experiments

We ran automated patch clamp experiments using a standard electrophysiology rig with four PatchStar micromanipulators on a universal motorized stage (Scientifica, Ltd). We used a peristaltic pump (120S/DV, Watson-Marlow) to perfuse the brain slices with buffer solution. The Multiclamp 700b amplifier (Molecular Devices) and USB-6221 OEM data acquisition board (National Instruments) to collect recordings. We used a pressure control box (Neuromatic Devices) to regulate internal pipette pressure as well as a custom machined chamber with a smaller side chamber for cleaning solution. We followed the cleaning protocol as suggested by [95], however we did not include rinsing in the cleaning protocol because recent literature found that there is no impediment to the whole cell yield or quality of recording [96]. We compared the state-of-the-art cross correlation method for pipette detection [72] to the CNN method presented here in two different sets of experiments. In order to remove extraneous confounding variables, none of the patch clamp experiments included the cell tracking algorithm used by Kolb et al. so that any variation due to cell tracking would not affect the success rates of the two pipette identification methods [72].

2.2.8 Statistical Analysis

To determine statistical significance in success rates, we used the Fischer's Exact Test. For the comparison between groups, we used a one-way analysis of variance (ANOVA) test, and a Tukey honestly significant difference (Tukey's HSD) test. To test for normality, we used a 2-sided chi squared test that combines skew and kurtosis to test for normality [97, 98].

2.3 Results

2.3.1 Validation of Pipette Position Identification

To determine if the network could accurately identify the pipette tip position over a brain slice, we tested the network on a set of 300 test images, manually annotated with ground truth positions. Representative test images of the pipette over a brain slice, with the CNN position indicated in red, are shown in Fig. Figure 2.1b. It is crucial that the CNN errors, $\vec{c}$, are smaller than the true pipette errors, $\vec{t}$, that accumulate during an experiment to ensure that the pipette position error will converge. To demonstrate that the CNN errors, $\vec{c}$, are smaller and more repeatable than the pipette errors from moving to the cleaning bath and back to the sample,$\vec{t}$, these two distributions along each axis are displayed in Fig. Figure 2.1c. The mean absolute errors and standard deviations of the CNN errors for each of the axes are shown in Table Table 2.2.

Table 2.2: CNN Error from Test Data Set

Error	$\vec{c}$ (μm)	$\sigma(\mu m)$
c_X	0.39	0.35
c_Y	0.39	0.37
c_Z	0.83	0.88
$\lvert\vec{c}\rvert$	1.13	0.88

To ensure that the CNN successfully corrected the pipette tip position, we evaluated the network's ability to converge using the previously described testing work flow. The magnitude of the true pipette error after 1-4 iterations in the XY plane ($|\vec{t_{xy}}|$) and Z direction ($|\vec{t_z}|$) are plotted in Fig. Figure 2.1d. While there was a significant difference between the first and second iterations (p = .001 Tukey;s HSD test), there was no statistical significant difference between the second and third iterations in the XY plane (p = 0.49 Tukey's HSD test). After the second correction, 62% of the attempts were within one standard deviation ($\pm 0.31\mu$m) of the target location in the XY plane (p = 0.016 D'Agostino test for normality, α = 0.05), and 86% of the attempts were within two standard deviations ($\pm 0.62\mu$m), as

indicated by the circles in Fig. Figure 2.1e. Since the network was able to correct the pipette tip to less than approximately half the diameter of a typical cell (10 μm) in the XY plane with only two iterations of the CNN, we only corrected the pipette position twice for implementation in automated patch clamp experiments. The discretization that is apparent along the y-axis is the step size of the micromanipulators, indicating we are approaching the stepper motor encoder resolution. In the Z direction, 64% of attempts were within one standard deviation (0.60μm) of the target location (p = 0.026 D'Agostino test for normality, α = 0.05) and 84% of the attempts were within two standard deviations (1.2μm), which is an acceptable range that we believed would not impair the ability of the pipette to find and patch clamp a cell. The accuracy in the Z direction was less crucial since the approach method is to descend the pipette from 15 μm above the cell.

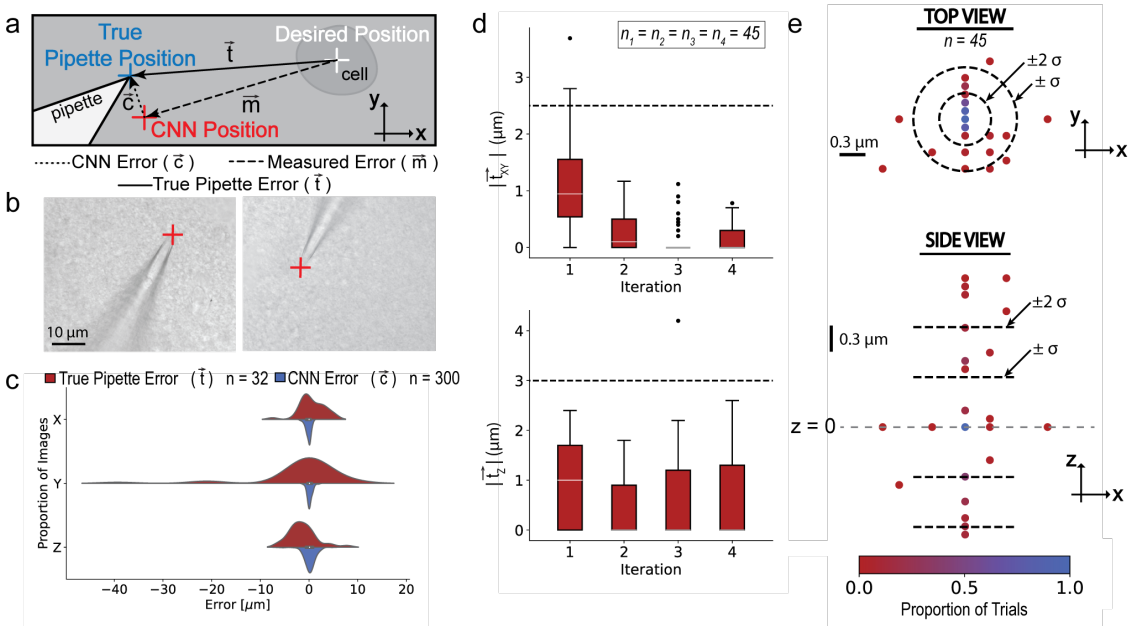

Figure 2.1: (a) Schematic of the error nomenclature used in this work. (b) Example images of the CNN identifying the pipette tip over a brain slice. (c) Error distribution of neural network testing data set n = 300 images (red) compared to the true pipette error after moving to the cleaning bath for n = 32 images (blue). (d) Convergence of true pipette error magnitude using the CNN as the measurement feedback in the *top*: XY plane and *bottom*: Z direction. The black dotted lines indicate appropriate error ranges for patch clamp experiments, at 2.5 μm in the XY plane (half the diameter of a typical cell) and 3 μm in the Z direction. (e) Spatial representation of pipette tip locations after the second iteration of using the CNN for correction in the *top*: XY plane and *bottom*: Z direction. Black dotted lines indicate the range of one and two standard deviations.

2.3.2 Automated patch clamp experiments

We compared the success rates of the CNN method and the state-of-the-art cross correlation method on pipette detection, cell detection, and whole cell recording. Success rates are defined as a fraction of all attempts using the same pipette detection method, independent of whether the previous steps were successful. Success is defined for each of the steps as follows: Pipette detection is considered successful when the pipette position can be identified and corrected based on that identification. Cell detection is considered successful when the pipette resistance increases 0.2 MΩ over three consecutive descending 1 μm steps. Whole cell patch clamp recording is defined by successful cell detection, gigaseal, and break-in. When using the CNN method, two corrections were done after the pipette is brought into the field of view, as previously described. All experiments were done over 5 days, using 8 slices from 5 mice. The numbers of attempts with each method are 32 and 36 for the cross correlation and CNN methods, respectively. These experiments were done independently, but prepared using the same protocols and solutions to reduce variability in slice health.

The pipette detection, cell detection, and whole-cell success rates using cross correlation were 66%, 59%, and 37% respectively (n = 32). The pipette detection, cell detection, and whole-cell success rates using the CNN were 100%, 92% and 64% respectively (n = 36). These results are summarized in Figure Figure 2.2a. A Fischer's Exact test of the results indicate that the CNN improved the pipette detection success rate by 52% (p = 8e-5 Fischer's Exact Test), the cell detection success rate by 54% (p = 0.001 Fischer's Exact Test) and whole-cell success rate by 70% (p = 0.05 Fischer's Exact Test). Moreover, the CNN method could reliably identify the pipette position regardless of the background noise in the image within 2.71 $\pm$ 0.30 seconds, 81% faster than the average time of the cross correlation method, as shown in Figure Figure 2.2b.

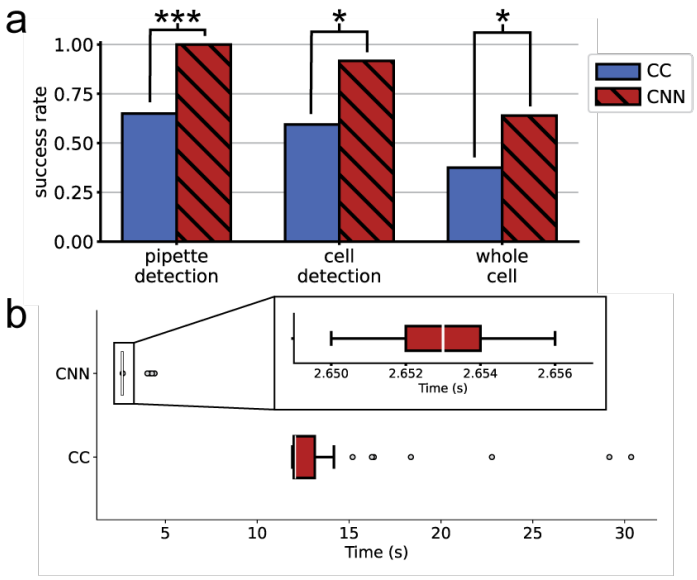

Figure 2.2: Comparing (a) pipette detection, cell detection, and whole cell success rates and (b) time required for cross correlation and CNN methods (n = 32 and n = 36 respectively). Using Fischer's Exact Test: * indicates P $\leq$ 0.05, *** indicates P $\leq$ .001

2.3.3 Electrophysiology Data

The patch clamp experiments done with the CNN method yielded both voltage and current clamp data comparable to the quality of a manual patch clamp expert. An example image of the pipette placed on the cell is shown in Figure Figure 2.3a. The whole cell recording protocol used was the same as that of [72]. The distributions of access resistance, membrane capacitance, and membrane resistance are shown in Figure Figure 2.3b. The mean access resistance for recordings performed with the CNN was 14.1 MΩ, well within the accepted range among manual patch clamp experts ($< 40M\Omega$) [72]. A representative current clamp trace and the corresponding input current injection are displayed in Figure Figure 2.3c. A voltage clamp trace is shown in Figure Figure 2.3d.

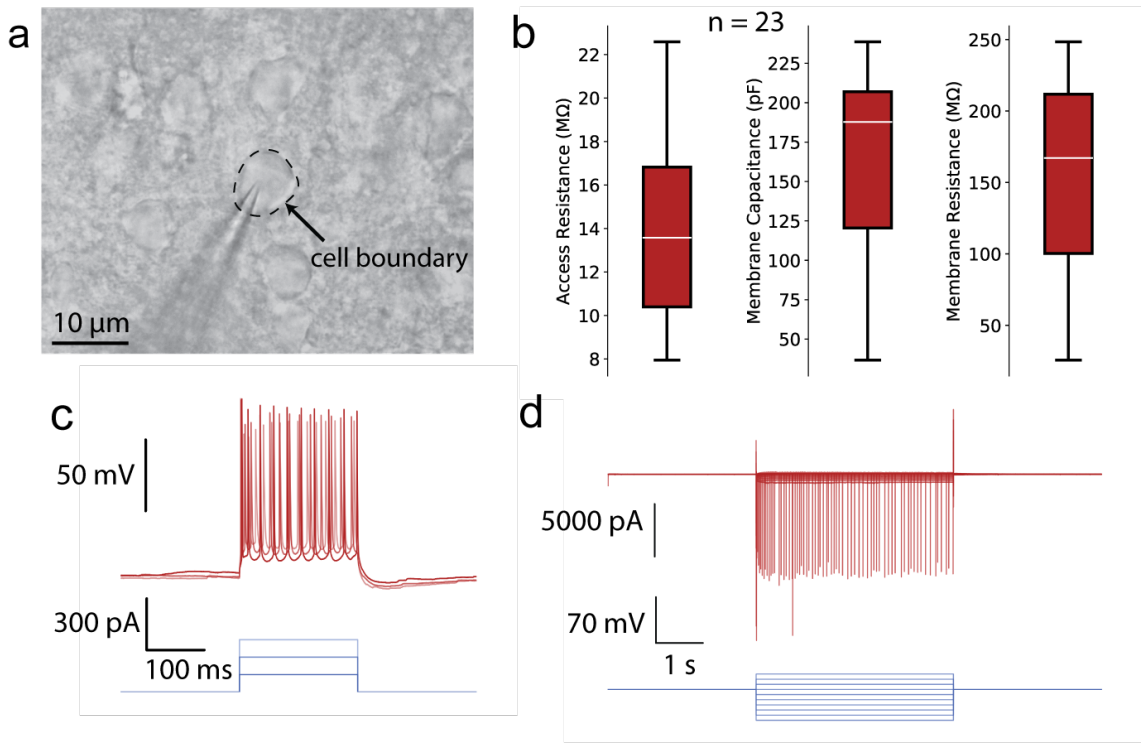

Figure 2.3: (a) Example image of a pipette on a neuron during a whole-cell recording. (b) Distributions of access resistance, membrane capacitance, and membrane resistance for n = 23 successful whole cell patch clamp recordings using the CNN. The white lines indicate the median, the width of the boxes indicates the first and third quartiles, and the whiskers indicate the range of the data. (c) Representative current clamp trace with current injection. (d) Representative voltage clamp trace.

2.4 Discussion

One of the primary disadvantages of using the previously reported methods for pipette detection is the lack of reliability. With the cross correlation method, the pipette tip could be identified for 66% of attempts (n = 32), failing due to the difference between the template image and the background noise from the brain slice [72]. The deep learning-based pipette detection method presented here offers an accurate and robust method for identifying the pipette tip position in automated patch clamp experiments both over a clear background as well as above a brain slice. Other methods of pipette tip identification have reported accuracy of $12.06 \pm 4.3\mu$m [82], $3.53 \pm 2.47\mu$m [81], and $0.99 \pm 0.55\mu$m [80]. We reduced the 3D positioning error, using two iterations of our CNN method, to $0.62 \pm 0.58\mu$m. The CNN can more reliably identify the pipette location in the XY plane compared to the Z axis. This difference in error distributions is likely due to the fact that small changes of the pipette position in the Z direction (moving into and out of focus) are less clearly observable when viewing the pipette under the microscope, especially when over a brain slice. However, despite this inherent ambiguity in the pipette tip position, the errors in the Z direction are still significantly lower than previously reported.

By training a CNN to correct the pipette tip position during automated patch clamp experiments, we improved the success rates of pipette detection to 100% compared to the 66% success rate for cross correlation. This ability to reliably correct the pipette every time it is in the field of view could be used for automatic calibration or real-time tracking of the pipette's location for optimization of autopatching protocols. This method also improved the cell detection and and whole cell success rates by 54% and 70% respectively compared to the success rates of the cross correlation method without use of cell tracking, demonstrating the importance of the accuracy and robustness of this crucial step in the autopatching process. Moreover, this CNN method without cell tracking performed similarly with cells 50- 60 μm deep (64%) to that of Kolb et al. (60%), who reported a 60% whole cell success

rate using cross correlation and cell tracking at the same cell depth [72]. Furthermore, the average time required to correct the pipette position using this CNN method is 81% less than the cross correlation method, averaging 1.6 seconds per iteration of the CNN identification and movement of manipulators, opening doors to real-time tracking of the pipette tip during automated patch clamp experiments.

There were several limits to this study. For one, we only used one micromanipulator manufacturer (Scientifica). While there may be different error distributions between various manufacturers, we anticipate that this method would still be effective if the modified ResNet101 architecture was trained with new images specific to the objective magnification and manipulator. Further, only pipettes with resistances in the range 3-5μm were used for training and testing since this range is standard for patch clamp experiments *in vitro*. Pipettes used for other applications, that are significantly narrower or wider, would need more training data to ensure the network could reliably identify the tip's new geometry. Similarly, use with other objective magnifications or pipettes at different angles would also require collecting new training data. This paper provides a set of parameters that can help streamline retraining this model, however retraining the model with a new set of training data may present as a substantial obstacle for some groups.

Notably, we omitted the use of cell tracking in the automated patch clamp experiments so that (1) we could isolate errors and measure success rate independently of the cell tracking algorithm and (2) to reduce the computational cost of correcting the pipette tip and the cell at the same time. Future work could certainly integrate a CNN with a cell tracking algorithm to simultaneously monitor and correct the pipette location with respect to the cell, potentially leading to even greater whole cell success rates than previously reported. Moreover, this dual-monitoring could be used to continuously monitor the access resistance and correct the pipette position to maintain this resistance during longer duration experiments. Further, the combined monitoring of the cell and pipette positions may be of great use in multi-electrode automated patch clamp experiments, in which the brain tissue moves more

from the simultaneous movement of multiple pipettes in the tissue. This work represents another significant step towards unmanned robotic patch clamp development.

CHAPTER 3

DEEP-LEARNING BASED AUTOMATED NEURON DETECTION

This work has been published in Scientific Reports [99].

3.1 Introduction

One of the most crucial initial steps in the patch clamping process is identifying a healthy cell. The edges of a healthy neuron under DIC are often unclear and vary widely in shape and size. Moreover, the milieu of brain tissue not only consists of neurons, but also cerebrospinal fluid, blood vessels, and glia, among other extracellular content which induce significant light scattering under differential interference contrast (DIC), an optical technique widely used for observing unstained biological samples. While fluorescence microscopy may be used for identifying somas in acute slice patch clamp experiments, it is not always practical since it requires the use of dyes or genetically engineered production of fluorophores [100]. Rather, it is often desirable to image label-free, yet optically transparent samples which require the use of DIC.

Since this is such a critical task, automation of the cell identification and selection process is a difficult and necessary step towards completing full automation of patch clamp. Research groups enabling the automation of patch clamp have alluded to the potential benefits of automating this task, though the problem is not yet fully resolved [101, 73, 102]. Koos et al. have recently shown a CNN that identifies somas under DIC, though their network required substantial time and over 6,000 annotated neurons for training [80]. In this study, we aimed to achieve similar accuracy on a smaller, faster CNN that can quickly nominate cells for patch clamp experiments. Our deep learning-based method, quantified by F1 scores and mean average precision (mAP), is comparable to published work on cultured cell identification and other deep learning based solutions for cell detection. Thus,

we show that transfer learning using the YOLOv3-CNN architecture can require minimal training resources and enable fast, accurate neuronal detection for images gathered on live, acute brain slices.

3.2 Methods

Convolutional Neural Network: YOLOv3

The training, validation, and test data sets consisted of 1280x1024, 8-bit raw images of acute slices under DIC. Within the training and validation data sets, 369 original, raw images were used with a total of 1138 annotated neurons. For the trained CNN test data set, a smaller set of 37 images was used containing 107 annotated neurons. Since we are using transfer learning on a pre-trained model, a smaller data set for training and validation is appropriate to obtain sufficient accuracy.

We utilized the default architecture of the YOLOv3 neural network, most notable for its speed and accuracy of detection [103, 104]. The initial model was pre-trained on the Imagenet data set [104]. The final 3 layers were initially trained with our custom acute brain slice data set for 10 epochs before all layers were unfrozen and the entire network was trained on the data set for 40 more epochs for a total of 50 epochs. If loss reached a steady state value, the training would stop early.

Both the unaltered image and the enhanced image data sets were randomly divided into a training and validation set at a 10:1 ratio. The input image resolution was set to 416x416 pixels. While downsampling the images to 416x416 introduces some unintended artifacts of reduced resolution, there is a desired trade-off between computational time and accuracy. Secondly, the dimensions of the input image are resized while maintaining the image aspect ratio. For example, the longer dimension, 1280, is scaled to 416 The remaining pixel areare4iujk is black pixels. The YOLOv3 network architecture consists of a backbone network called Darknet-53, an up-sampling network, and the detection layers called YOLO layers [103, 104].

3.3 Results

The unaltered trained network was trained on images without preprocessing. Conversely, the enhanced trained network was trained on images enhanced with histogram equalization [105]. The mean average precision and F1 scores of both networks are summarized in Table 3.1 and Table 3.2, respectively.

Table 3.1: Mean average precision of unaltered and enhanced trained networks tested on unaltered and enhanced input images.

	Unaltered Input	Enhanced Input
Unaltered Trained Network	77.00%	54.62%
Enhanced Trained Network	59.10%	71.93%

Table 3.2: F1 score of unaltered and enhanced trained networks tested on unaltered and enhanced input images.

	Unaltered Input	Enhanced Input
Unaltered Trained Network	0.80	0.67
Enhanced Trained Network	0.61	0.76

The training loss and validation loss for both networks shown in Figure 3.1a highlight the neural network quickly fitting to the training set and converging towards a steady-state of trained weights. While the results of the models over enhanced images provide relevant information over the precision of the networks, generally, preprocessing each frame during a real-time live-imaging experiment would cause latency issues so further accuracy and confidence score distributions are studied using only the unaltered test images data set. As seen in Figure 3.1b, the mean accuracy of the unaltered net was 0.703 ± 0.296 while the enhanced net was 0.378 ± 0.306, student's t-test p¡.001. Figure 3.1c shows the confidence scores distribution for unaltered and enhanced networks tested on the unaltered data set test images. The notches represent the confidence interval around the median, 0.599 and 0.711, respectively. Examples of each network identifying neurons in a test image can be found in Figure 3.1d and Figure 3.1e.

Although our average reported inference time for an image was 580 ± 147 ms, this can be attributed to testing the trained models on the CPU of the notebook PC described in the Methods section. Average inference time testing the trained models on the GPU described in the Methods section was 56.7 ± 1.43 ms. This provides an 18 frame per second real-time detection rate. Furthermore, the training time for each of the models was 18 minutes.

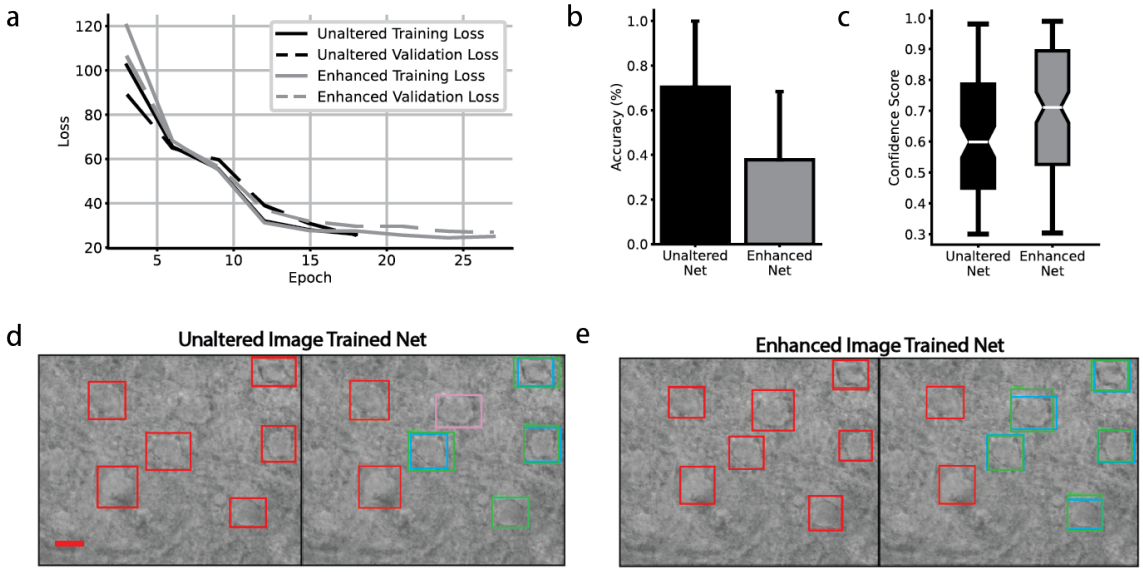

Figure 3.1: (a) Convergence on training and validation loss with respect to number of epochs. Black lines represent the unaltered trained model losses, and gray represents the enhanced trained model losses. Solid lines represent training loss, and dashed lines represent validation loss. (b) The bar chart shows mean$\pm$SD comparison of the average accuracy between the unaltered net and enhanced net on the unaltered data set test images. A student's t-test (α=0.05) acknowledges that the difference between the means is statistically significant; t(36)=5.12, p¡.001. (c) Box plot comparison of the confidence scores distribution for unaltered and enhanced networks tested on the unaltered data set test images. The notches represent the confidence interval around the median using a Gaussian-based asymptotic approximation. The ends of the boxes are at the first and third quartiles while the whiskers represent the minimum and maximum confidence scores. (d-e) Example of both networks identifying neurons in a test image. *left*: initial prediction (red) of neurons. *right*: bounding boxes for annotation (blue), correct prediction (true positive—green), incorrect prediction (false positive—red), and undetected neurons (false negative—pink). Scale bar: 10 μm

To validate the health of the identified cells, we performed a set of patch clamp experiments on neurons identified by one of the trained neural networks. We chose to use the unaltered trained network since it demonstrated the greatest mAP and F1 scores. The av-

erage access resistance was 29.25 MΩ, with 8 of 9 patched cells within the accepted range among patch clamp experts (<40 MΩ) [101].

3.4 Discussion

In this study, we developed a method for detecting neurons in acute, rodent brain slice for anticipatory use towards assisting patch clamp experiments. We then validated the method's ability to identify healthy cells by patch clamping neurons identified by the best performing network. The application of this neural network in the context of patch clamp has great potential to help fully close the loop towards complete automation of the patch clamp technique on acute brain slices and reduce the need for immense training and skills required for manual identification of healthy cells. The YOLO network architecture's speed and accuracy are conducive for nominating healthy neurons in acute brain slice in real-time with a display and detection rate of 18 frames per second. Thus, this neuron detection method is a tool not only valuable for initially identifying neurons for patching, but it could also provide tracking of the cell location as the slice is moved during an experiment to aid in throughput and quality of the recording.

CHAPTER 4

PATCH-WALKING: FINDING SYNAPTIC CONNECTIONS

This work is under review at eLife.

4.1 Introduction

Scientists aim to understand the mechanisms governing cognitive functions by measuring brain activity at the level of individual neurons and elucidating the complex synaptic connections that underlie neural networks, despite significant challenges in their identification, measurement, and comprehension. In the field of connectomics and synaptic physiology, several groups have developed methods for obtaining semi-automated patch clamp recordings of synaptically connected neurons [106, 107, 108, 109, 110]. In all previous efforts, both manual and automated, in which multiple pipettes (referred to as multi-patching) are used to probe for synaptic connections, the experimental approach has involved (1) obtaining as many simultaneous recordings as possible, (2) probing their connections, and then (3) retracting all pipettes.

Recognizing how much effort and skill is necessary to obtain many simultaneous recordings, coupled with the advantages of pipette reuse and automation, we hypothesized a novel approach. If instead of retracting all pipettes, perhaps just one of them could be cleaned and reused to obtain a new whole cell recording while maintaining the others. Thus, with one new patch clamp recording attempt, many new connections can be probed. By placing one pipette in front of the others in this way, one can "walk" across the tissue, which we term "patch-walking." Thus, in this work, we introduce the theory, methods, and experimental results for a fully automated in vitro approach with a coordinated pipette route-planning to "patch-walk" across a brain slice. We demonstrate efficiently recording dozens of neurons using a two-pipette apparatus for finding synaptic connections. Here, we show that this

approach, as compared with the traditional approach, increases the rate of potential neurons probed, decreases experimental time, and enables sequential patching of additional neurons.

4.2 Methods

4.2.1 Patch-walking visualized

To visualize the advantage of patch-walking over the traditional method, these two equations can be represented as a matrix of potential probed connections. For example, the total number of possible connections using the traditional method and patch-walking for a two pipette apparatus is depicted in Figure 4.1A and B, respectively. Using these equations, patch-walking is always preferable in practice for $n > p$. Furthermore, one can expect the improvement in number of connections probed to approach double as n approaches infinity. For practical cases (apparatus with 2-8 pipettes), patch-walking yields 80-92% more probed connections, or efficiency, for experiments with 10-100 cells than the traditional synaptic connection searching method.

4.2.2 Patch-walking algorithm

The patch-walking algorithm is depicted schematically in Figure 4.2. At the beginning of each patch-walking experiment, cells are first selected by the user. For each slice experiment, we selected 8-10 healthy cells located 20-100 um below the surface of the tissue. These cell locations with three dimensional coordinates are stored in a cell queue for subsequent patch attempts. From these cell coordinates, the robot computes the distance between the pipettes' respective home positions and each cell.

We define a paired recording as a pair of cells which are simultaneously patch clamped using the patch-walking experimental method. We define probed connections as twice the number of paired recordings, because the connections can be bi-directional. We define possible connections as the theoretical upper limit of probed connections given a number

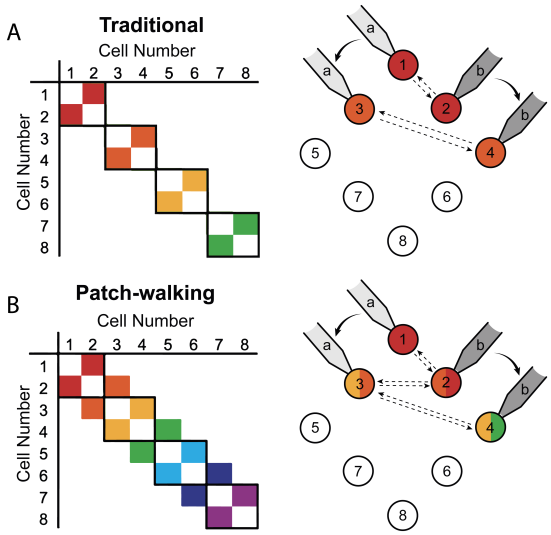

Figure 4.1: A-B. Schematically, for patch clamp apparatus with two pipettes in search of synaptically connected neurons to record; colored squares represent connections that can be probed using the traditional approach (A) as compared to patch-walking (B). In this schematic, n=8 cells were patched by p=2 pipettes, either in groups of two (A), which yields two possible connections, or by walking across the tissue (B), which yields almost double the number of possible connections.

of pipettes and number of cells recorded. Probed connections is, practically speaking, less than possible connections since patch clamp yield is 30-80% based on our experience with the PatcherBot, depending on sample preparation and tissue and cell type.

4.2.3 Connectivity Testing

We tested for connectivity in a manner similar to that done previously by Peng et al [111] and the Allen Institute for Brain Science [110]. To perform connectivity testing between two simultaneously patched neurons, we performed the following procedure. The BNC cables were manually moved from the NI DAQ to the Digitizer to enable Clampex control of the cells (rather than LabView). Two protocols were run in order to test for the two possible directions of connectivity. For each protocol, one pipette sent a stimulus in current clamp mode to elicit five action potentials at 20 Hz while the other pipette holding in voltage clamp recorded post-synaptic currents, held at -70 mV. Following this bi-directional

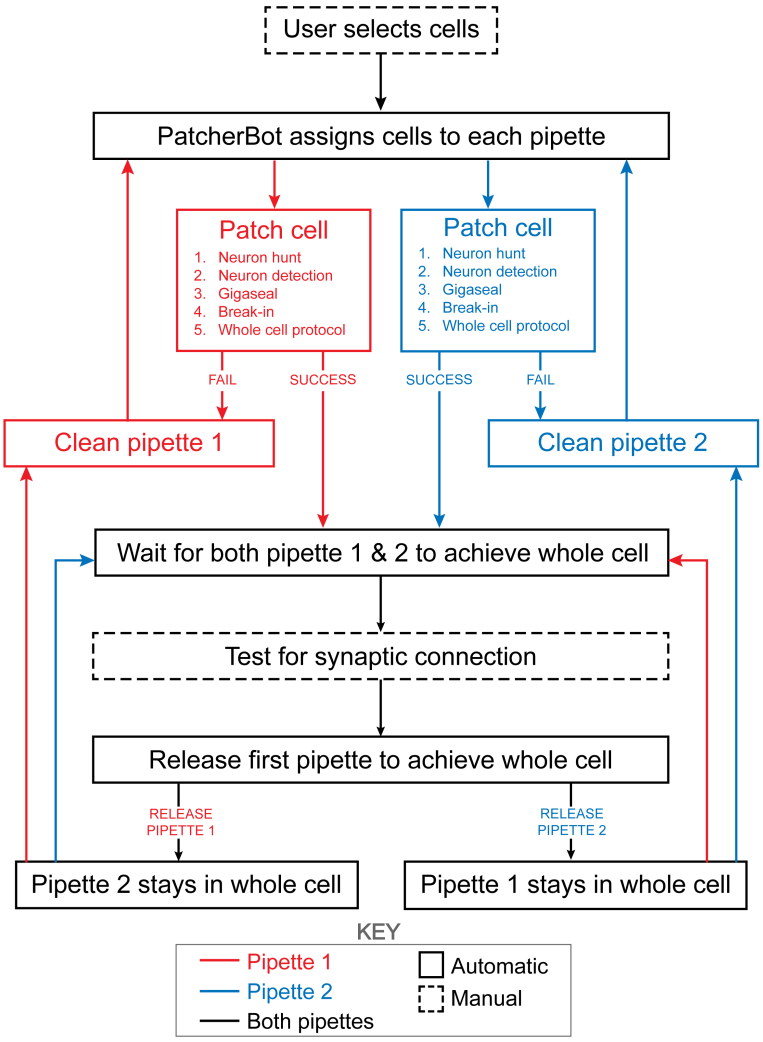

Figure 4.2: Schematic of the patch-walking experimental workflow. The patch-walking process begins with selection of cells by the user. The Patcherbot then assigns cells to each pipette based on their distance to the pipettes' home positions. Each pipette works in parallel, only working independently during steps which require the camera and stage (ie neuron hunting, neuron detection). Once a pipette has achieved these steps successfully, the stage and camera are designated to the other pipette. If the pipette failed the patch attempt, it is cleaned and reused. Once both pipettes achieved whole cell configuration, they are tested for synaptic connectivity. In order to "patch-walk," the first pipette to achieve whole cell is released to clean and obtain a new whole cell recording.

measurement, the BNC cables were replaced manually to resume patch-walking.

4.3 Results

We performed patch clamp attempts on 136 cells from 7 animals over a corresponding 7 days, with 2-3 slices per animal. Out of 136 patch clamp attempts for both pipettes, we achieved 130 successful neuron-hunts (95.6%), 71 successful gigaseals (52.2%), and 71 successful whole cell recordings (52.2%). This is again comparable to previously reported automated patch clamp work such as Kolb et al. (51%), Wu et al. (43.2%), and Koos et al. (63.6% for rat, 37% for human) [80, 73, 72]. In addition, our success rates fall within the success range of manual users (30-80%) on differential interference contrast-based patch clamp systems [112]. Thus, coordinating the motion of the pipette via the patch-walking algorithm does not deteriorate the success rate.

A schematic representation of the experimental arrangement featuring dual patch pipettes in the primary visual and somatosensory cortices is shown in Figure 4.3A. In Figure 4.3B are histograms showing the distribution of the time it took to achieve a simultaneous recording (left, n = 44), the intersomatic distance between neurons that were patch clamped simultaneously (center, n = 44), and the time to achieve gigaseal for all cells (n = 71). In Figure 4.3C are the distributions of whole cell properties (capacitance, tau, input resistance, resting membrane potential, and access resistance) of all cells. We were able to achieve paired patch clamp recordings between two pipettes in an average of 12.6 ± 7.5 min as the pipettes walked across the slice. The average distance between two neurons for screened for connections was 91.6 $\pm$ 0.2 μm.

We demonstrate a connectivity matrix similar to those done by previous labs such as Peng et al. and the Allen Institute for Brain Science [107, 110]. Of the 71 whole cell recordings we recorded from the robot, we report a yield of 44 paired recordings using our patch-walking technique. In comparison, if we had screened the same 71 neurons for connections using the traditional method, we would have screened for 71/2 = 35 paired recordings. Therefore, our patch-walking algorithm screened for 9 more possible connec-

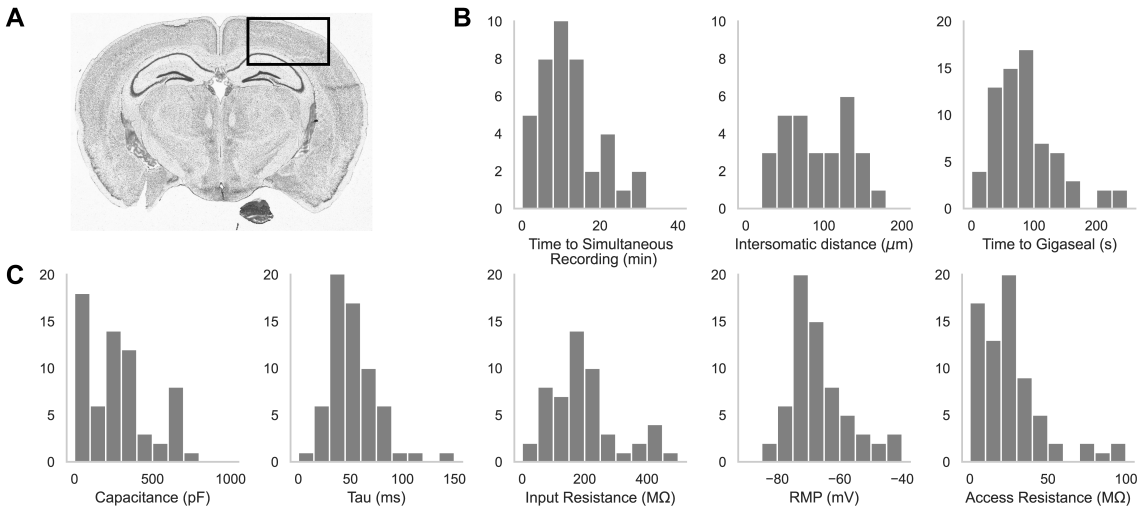

Figure 4.3: A. An image of a brain slice with a box highlighting the brain region used for experiments: the somatosensory and visual cortices. B. Histograms of patch clamp metrics: time to achieve simultaneous recording (n = 44), distance between neurons during paired recordings (n = 44), and time to achieve gigaseal (n = 71), access resistance (n = 71), and C. Whole cell properties of all cells recorded during patch-walking experiments (n = 71).

tions for the 71 neurons we tested. Of those 44 recordings, 29 paired recordings (i.e. 58 probed connections) passed quality control checks and were used to validate the efficiency of the patch-walking algorithm.

According to Perin et al [111], at an intersomatic distance of 91.6 $\pm$ 0.171 μm, the expected connection probability is 16.9% for each paired recording. Assuming they are independent, we would expect greater than 50% probability of getting at least 1 connection after just 3 paired recordings. According to binomial probability theory, we had a probability of 89% to find 3 connections with 29 paired recordings.

Figure 4.4 shows a connectivity matrix (as in Figure 4.1B), a spatial representation of the cells patched cells and connection probed, as well as a representative connection found between two cells. The matrix in Figure 4.4A shows the whole cell current clamp protocol described previously (black traces in leftmost column). During paired recordings, one cell would be stimulated in current clamp (traces along the diagonal). Recording color corresponds to a pair of cells tested for connectivity as in Figure 4.1A, where each color has

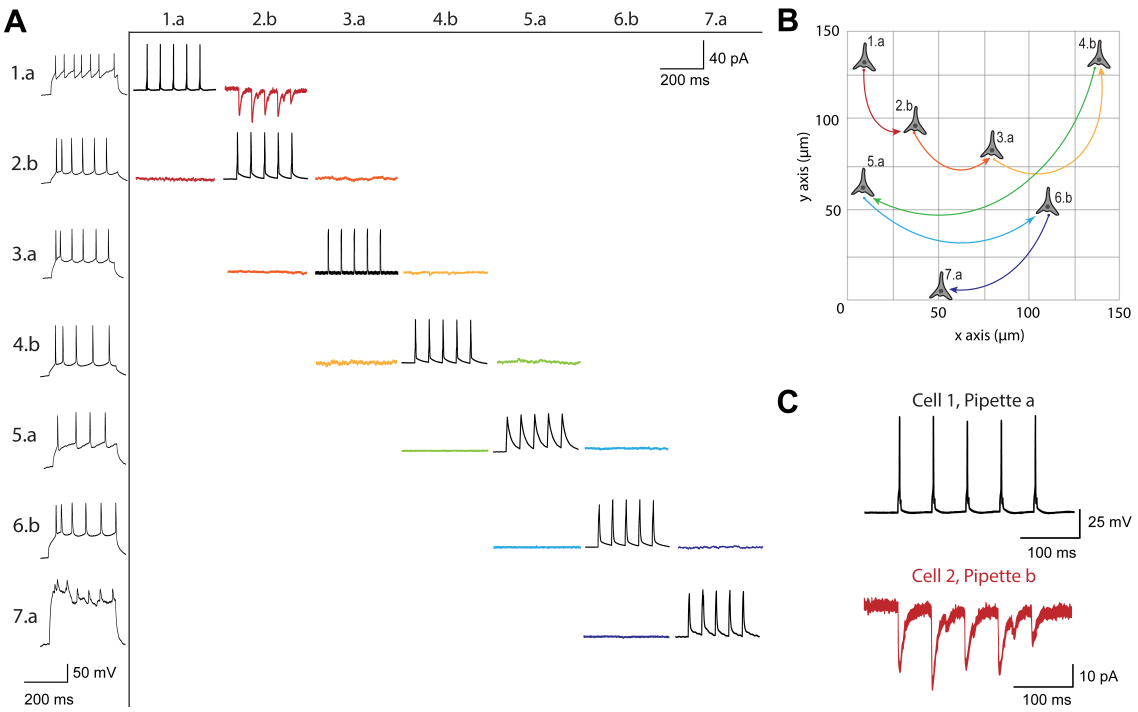

Figure 4.4: A. Matrix of voltage and current traces from 7 neurons in one acute brain slice recorded using the patch-walking algorithm for the robot. Left column shows the firing pattern of the recorded neurons. Cells are numbered such that the number represents the cell and the letter represents the manipulator (a or b). Scale bars: Horizontal 200 ms for firing pattern and connection screening. Vertical 40 mV for action potentials, 50 pA for postsynaptic traces. B. Patch-walking scheme of all neurons from the experiment matrix in (a). The curved lines between neurons represent probed connections in the matrix in (A). C. The probed connection from the connectivity matrix in (A). The stimulus was sent to cell 1 (black) and the response from cell 2 (red) was recorded and averaged over three sweeps.

two traces because each pair of cells can be connected bidirectionally. The nomenclature for each row and column is $n.p$ where n represents the cell number, in this case ranging from 1-7, since 7 total cells were patched between both pipettes, and p labeled either a or b represents each of the two pipettes.

The representative connection shown in more detail in Fig Figure 4.4C was found between cells 1 and 2, with pre-synaptic cell 1 (black) stimulated and cell 2 (red) recording in voltage clamp the post synaptic currents elicited.

4.4 Discussion

We introduce a variation on the multi-patching technique which we termed patch-walking. Patch-walking enables, theoretically, almost twice the number of connections to be probed on a patch clamping apparatus for a given number of cells patched and pipettes on the rig. We recommend this method for those searching for local synaptic connections using a rig with a small number (e.g, two) of pipettes, such as we have shown. Furthermore, patch-walking provides other advantages: it damages the tissue less between probed connections, decreasing the chance of severed connections, it saves time between experiments since only one pipette is moved at a time, and it enables more recordings from a tissue before cell death which is advantageous for studying rare tissues such as human brain samples.

For scaling patch-walking beyond the apparatus described here, we caution that one must take into account pipette collisions and choose cell-pipette assignments carefully. Future work to improve upon patch-walking could include developing an optimal route-planning path such as the Monte Carlo Tree algorithm as a strategy to optimize the pipette-cell assignments, considering (1) spacing pipettes apart in order to avoid collisions between the fragile glass pipettes while (2) maximizing the probability of a connection. Specifically, we would recommend a threshold of inter-cell distance to be less than 200 μm in order to have at least a 10% probability of connection according to Perin et al. [111].

Out of the 29 paired recordings, we found 3 synaptic connections. While this number of connections is lower than predicted according to Perin et al. [108] based on the intersomatic distances between these cells, we hypothesize that this is most likely due to biological variation.

While the patch-walking method provides an efficient means to probe for synaptic connections using two pipettes, introducing additional pipettes presents notable challenges. Specifically, as pipettes maneuver into and out of the brain slice, tissue deformation often disturbs any pipettes in whole cell configuration.

CHAPTER 5
RAPID ENZYMATIC CLEANING OF PATCH PIPETTES

5.1 Introduction

Historically, the patch clamp technique has required pulling and filling a new pipette after every attempt, even after failed attempts. Changing pipettes between attempts adds significant time to each experiment. This is a major concern when samples, such as acute brain slices, are only viable for a limited time. In 2016, Kolb et al. [95] discovered that patch pipettes can be cleaned and reused immediately, enabling users to begin a new patch attempt within one minute of the last attempt. This method consisted of automatically removing the patch pipette from the sample bath, dipping the pipette into Alconox, a detergent commonly used to clean glassware, cycling between positive and negative pressure inside the pipette, rinsing the pipette with artificial cerebrospinal fluid (aCSF) using a similar pressure profile, and returning to the sample for additional patch attempts. This approach has been used by several groups

Here we show that the pipette can be cleaned and resused with 2% w/v Tergazyme, a detergent that enzymatically cleans the tip of the pipette with pressure changes. Further, we show that the cleaning process works without the rinsing step and there is no effect on recording quality.

5.2 Methods

My contribution to this work demonstrated that pipettes could be cleaned and reused with Tergazyme, while omitting the rinsing step, in acute brain slices.

Coronal brain slices (300 μm) were prepared from 3-4 week old C57BL/6J mice. Automated patch clamp experiments were performed using the patcherbot as described in

[72]. The fully automated cleaning protocol begins after a failed patch attempt or after a successful whole cell recording. The steps taken by the LabVIEW program are as follows:

1. Retract pipette to ”safe” position.
2. Move pipette to ”above the cleaning bath” position
3. Move pipette to ”cleaning bath” position
4. Cycle pressure inside pipette: -345 mbar for 5 s, repeat -345 mbar for 1 s then +700 mbar for 1 s five times, +700 mbar for 5 s.
5. Retract pipette from cleaning bath to ”above the cleaning bath” position.
6. Return to ”safe position.
7. Begin next patch attempt.

5.3 Results

Out of 34 total attempts, 23 whole cells were achieved using the patcherbot. As shown in Figure 5.1A, the success rate as a function of reuse does not deteriorate even after 10 attempts. The yield for a single pipette over 10 attempts is shown in Figure 5.1B. Representative recordings are shown in Figure 5.1C-D, demonstrating no deterioration of recording or cell quality.

5.4 Discussion

Here I show that the rinsing step is unnecessary for cleaning and reusing pipettes when using the 2% w/v Tergazyme solution. Over 34 attempts, the whole cell success rate and quality of recording as a function of number of reuses were not adversely affected.

One hypothesis for why this is true is that the pipette must be in the bath, but not in contact with the cell, during the pipette correction and neuron hunting stages. During this

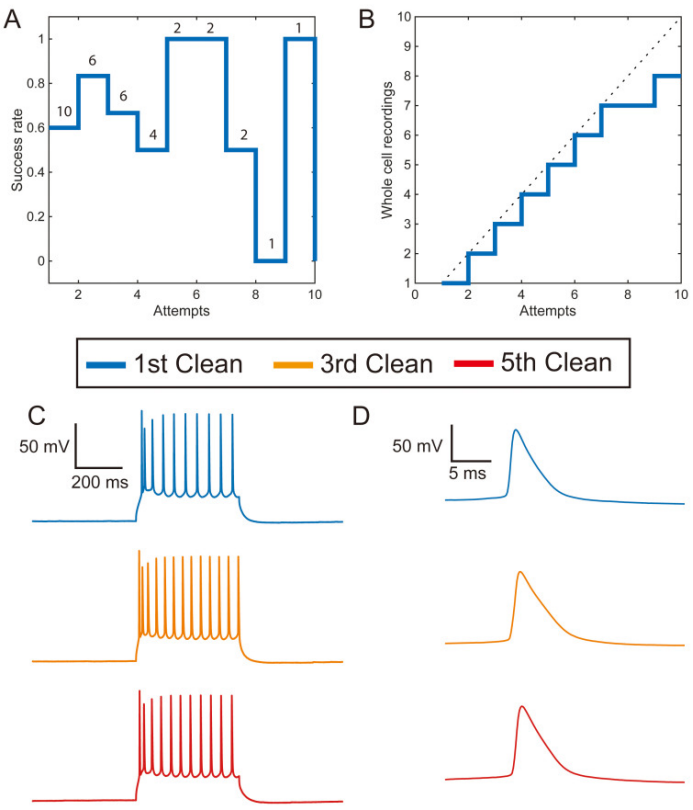

Figure 5.1: A. Whole cell success rate does not decrease as a function of number of cleans. The number of pipettes used is shown above the attempt number. B. Whole cell yield for a single pipette with 2% w/v Tergazyme solution without the rinsing step. C. Representative current clamp recordings from three different neurons using the same pipette. D. Enlarged action potentials from C.

time, the perfusion of aCSF over the sample may ”rinse” any remaining Tergazyme on the tip of the pipette. Thus, there is no measurable effect on whole cell quality. Another potential explanation is simply that the volume of cleaning solution that remains on the pipette after the cleaning step is too small to affect the success rate or quality of whole cell recordings even after multiple reuses.

The idea of cleaning and reusing pipettes has challenged traditional practices in the field of single cell electrophysiology. Here, the idea is pushed even further, wherein the rinsing step may be rendered obsolete, thereby streamlining experimental workflows and potentially enhancing overall efficiency and productivity in neuroscience research.

CHAPTER 6

REGIONAL EMERGENCE OF PV-INTERNEURON EXCITABILITY CHANGES

6.1 Introduction

Alzheimer's disease (AD) is a devastating neurodegenerative condition characterized by progressive cognitive decline and memory loss. AD is hallmarked by the accumulation of amyloid-beta plaques and tau protein tangles in the brain as well as neuronal damage [13]. Initially presenting with mild symptoms, AD gradually worsens over time, affecting various cognitive functions such as language and executive function, significantly impairing daily functioning and quality of life. As the leading cause of dementia, AD poses significant challenges for healthcare systems globally, necessitating urgent attention and innovative approaches to diagnosis, treatment, and care [14]. The disease's prevalence has reached epidemic proportions, impacting millions worldwide and placing a heavy burden on healthcare resources and caregiver networks, a burden expected to escalate with aging populations and increasing life expectancy [13, 12].

The prevailing theory in AD research has long revolved around the amyloid and tau hypothesis, positing that the accumulation of amyloid-beta plaques and tau tangles in the brain is the primary driver of neurodegeneration and cognitive decline in AD [9, 10, 11]. According to this hypothesis, the aggregation of these proteins leads to neuronal dysfunction, synaptic impairment, and ultimately cell death, resulting in the characteristic cognitive deficits observed in AD patients [18, 19]. While this hypothesis has provided valuable insights into the molecular underpinnings of AD pathology and guided much of the drug development efforts in the field, it has also faced significant challenges and limitations [32]. Despite extensive research and clinical trials targeting amyloid and tau pathology, no disease-modifying therapies have emerged, raising questions about the adequacy of the

amyloid and tau hypothesis in fully explaining the complex pathophysiology of AD.

In recent years, there has been growing skepticism and critique surrounding the traditional paradigm of AD pathogenesis, particularly regarding the exclusive focus on amyloid and tau pathology. Critics argue that while amyloid and tau may play significant roles in AD pathophysiology, they may not fully account for the heterogeneity of clinical presentations and disease progression observed in AD patients [113, 114]. Critics also point to emerging evidence suggesting that other factors, may contribute to the pathophysiology of AD, necessitating a shift in focus towards alternative mechanisms to develop more effective therapeutic strategies. These alternative mechanisms may include aberrant neuronal circuitry, synaptic dysfunction, neuroinflammation, and impaired clearance mechanisms, among others [114, 11].

In particular, evidence from both animal models and clinical studies provides compelling support for the involvement of neuronal circuit dysregulation in AD [34, 35, 41]. Several clinical studies indicate that there is increased brain activity in both sporadic as well as familial AD [115, 116, 117, 118, 119]. Animal models of AD have revealed alterations in neuronal network activity preceding the onset of classical pathological hallmarks, such as amyloid-beta deposition [37, 38, 39, 40, 41]. This excitability has been hypothesized to be a result of disrupted balance in excitatory and inhibitory neurotransmission [42]. In the context of AD, disruptions in the function and connectivity of GABAergic interneurons, which are characterized by their production of the inhibitory neurotransmitter GABA, are proposed to contribute to circuit hyperexcitability and cognitive impairment [51, 52, 53, 54]. This hypothesis posits that alterations in inhibitory signaling lead to imbalances in excitatory-inhibitory neurotransmission, thereby perturbing the delicate equilibrium of neural circuit activity and potentially AD progression.

Observations from animal models provide evidence for the involvement of PV interneurons, a sub-type of GABAergic interneurons, in AD [51, 55, 56]. Animal models have demonstrated alterations in PV interneuron function and connectivity preceding the on-

set of overt cognitive symptoms and pathological changes, suggesting their potential role in early disease mechanisms [57, 58, 59]. Understanding the regional and temporal emergence of interneuron dysfunction is crucial for deciphering the complex pathophysiology of AD and identifying potential therapeutic targets. Moreover, temporal changes in interneuron function and connectivity dynamics may underlie the progressive nature of cognitive decline in AD, with dysfunction manifesting at different disease stages. By elucidating the spatiotemporal dynamics of interneuron dysfunction, crucial insights into the progression of AD pathology can be revealed, potentially identifying critical windows for intervention.

To study these interneurons, there is a myriad of animal models which would provide valuable insight. Often, transgenic models are used to study AD, however they are susceptible to potential artifacts of hAPP [120, 121, 122]. To overcome this, we studied a humanized amyloid precursor protein knock-in model of AD [20]. This AD model contains three genetic mutations (Swedish, Arctic, and Austrian) to the APP gene, which results in progressive Aβ pathology as well as neurodegeneration and expected behavioral phenotypes [20]. As a control, we used the B6J hAβ strain, which contains a mutant APP gene that encodes humanized Aβ. By choosing this control strain, we aimed to determine whether changes in excitability are a result of hAβ or the genetic mutations in the knock-in model. We investigated the properties of PV interneurons and excitatory neurons across several cortical brain regions at an early time-point in disease progression. We hypothesize that the emergence of PV interneuron excitability changes will emerge in a similar pattern to the emergence of amyloid plaques in humans [123]. Notably, this patterning is also evident across several mouse models [124]. In total, we recorded from cells in the entorhinal cortex, medial prefrontal cortex, visual cortex, and motor cortex, representing two regions which are implicated in early AD and two regions which are likely unaffected in early AD.

The entorhinal cortex (EC) is one of the first brain regions to exhibit early neurodegeneration and neurofibrillary tangles (NFT) in AD [125, 126, 127]. Furthermore, recent evidence has suggested there may be altered excitability in this brain region in early AD in

humans [127] as well as in several mouse models [128, 129]. Thus, we hypothesized that there would be significant PV interneuron hypoexcitability in the entorhinal cortex. With this hypoexcitability of inhibitory cells, we predicted a corresponding hyperexcitability of excitatory neurons.

In general, the medial prefrontal cortex (mPFC) plays an important role in decision making and action, as well as motivation and emotion, among other higher-level brain functions [130]. The medial prefrontal cortex (mPFC) can be divided into three major regions: the anterior cingulate cortex (ACC), the prelimbic (PL) cortex, and the infralimbic (IL) cortex. In the context of AD, the mPFC has been implicated in early disease progression [131], specifically hyperexcitability of excitatory neurons [132, 133]. Due to this hyperexcitability, we hypothesized that PV interneurons would be hypoexcitable.

The visual cortex and motor cortex represent brain regions which are not suspected to be vulnerable in early AD. We thus predicted that these regions would exhibit no changes in PV interneuron or excitatory neuron excitability. We recorded from cells in these regions to determine whether the excitability of PV interneurons is altered across the entire cortex, or if it is a regional effect in this AD mouse model.

Since the interneuron hypothesis is based on the idea that PV interneuron dysfunction emerges in a region-specific way, and likely precedes amyloid plaques, this study will address an early time point in disease progression (i.e. before plaque formation and behavioral changes). By systematically investigating the regional dynamics of interneuron dysfunction, this work aims to quantify both the passive and active intrinsic properties of PV interneurons to determine if deficits in these cells are a result of AD genetic mutations. This knowledge will not only enhance our fundamental understanding of AD pathogenesis but also guide future development of more effective diagnostic and therapeutic strategies.

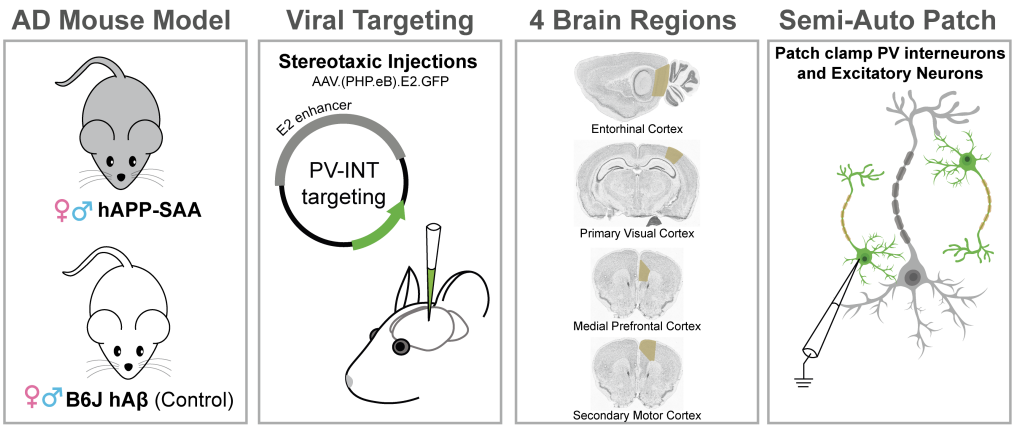

Figure 6.1: Schematic of the experimental approach: (1) Use a mouse model of AD and corresponding control line (2) Target PV interneurons with an adeno-associated virus (AAV) via stereotaxic injection (3) Choose 4 brain regions to study PV cell activity (4) Use semi-automated patch clamp to record from green fluorescent protein (GFP)-tagged PV interneurons and excitatory neurons.

6.2 Methods

6.2.1 Alzheimer's Disease Mouse Model

The human amyloid precursor protein knock in model (App^{SAA}) mouse model of AD was used (Jax Strain #034711[20]). The B6J hAbeta line (Jax Strain #033013) was used as a control.

6.2.2 Stereotaxic viral injections

Mice were injected with AAV(PHP.eB).E2.GFP at 6-8 weeks old via streotax (David Kopf Instruments). 300 μL was injected over the duration of 10 minutes + 5 minutes to prevent backflow (Hamilton Neuros Syringes) at the steretaxic coordinates in Table 6.1. Skin was sutured and mice were monitored during recovery from anesthesia under a heat lamp. Mice received SR buprenorphrine for pain relief. Mice were checked for wound healing for 3 days post operation.

Table 6.1: Stereotaxic coordinates (in mm) by brain region.

Brain region	**A/P**	**M/L**	**D/V**
LEC	-4.5	3.4	2.5
mPFC/M2	1.7	0.25	2.5
V1	-2.79	2.5	1

6.2.3 Acute brain slice preparation

All animal procedures were done in accordance with the US National Institutes of Health Guide for the Care and Use of Laboratory Animals and the Georgia Institute of Technology animal care committee's regulations. Mice were anesthetized with 4% isoflurane and decapitated. Brain slices (300μm) were prepared (Leica VT1200 Vibratome) in ice cold cutting solution (in mM: 25 NaH CO_3, 10 Dextrose, 75 Sucrose, 87 NaCl, 2.5 KCl, 1.25 NaH_2PO4, 1 $CaCl_2$, 2 Mg_2). Slices incubated in 33°C recording solution (in mM: 26.2 NaH CO_3, 11 Dextrose, 28.6 NaCl, 2.5 KCl, 1 NaH_2PO_4, 1.5 $CaCl_2$, 1.5 $MgCl_2$) for 30 minutes and at 24°C for 15 minutes before the experiment. Solutions were oxygenated with 95% Oxygen/ 5% Carbon Dioxide during the length of the experiment.

6.2.4 Semi-automated electrophysiology

A standard electrophysiology setup (SliceScope Pro 3000, Scientifica Ltd) with PatchStar micromanipulators at a 24°approach angle was used for all electrophysiology recordings. We used a 40x objective (LUMPFLFL40XW/IR, NA 0.8, Olympus) and Rolera Bolt camera (QImaging), illuminated under DIC with an infrared light-emitting diode (Scientfica). A peristaltic pump (120S/DV, Watson-Marlow) perfused the brain slices with recording solution, as described above. A pressure control box (Neuromatic Devices) regulated internal pipette pressure as well as a custom machined chamber with a smaller side chamber for cleaning solution.

Internal solution (in mM: 138 K-gluconate, 2 KCl, 10 HEPES, 4 Na_2ATP, 0.5 Na_2GTP, 4 $MgCl_2$, 3 L-Ascorbic Acid) was thawed on ice and filtered (0.2 μm) each day. Borosili-

cate glass pipettes with internal filament were filled with 5-10 μL of internal solution. Automated cleaning of the pipette between patch attempts was implemented with LabVIEW, as in [96]. 2% w/v Tergazyme solution was used to clean the pipette. The rinsing step was not included.

Cells were injected with current to maintain the membrane potential at -70 mV. For each cell, the following protocols were run:

- a voltage clamp membrane test, to initially estimate the passive properties of the cell
- a current clamp protocol with a depolarizing step -20 pA followed by a series of hyperpolarizing 2 pA/pF steps from -2 pA/pF to 30 pA/pF, normalized to the estimated capacitance of the cell
- a voltage clamp protocol of continuous (gap-free) recording for 90 seconds, setting the holding potential of the cell to -70 mV

Recordings with access resistance less than 20 MΩ and holding current magnitude less than 200 pA were considered good quality recordings for this analysis. Pipette capacitance was neutralized and access resistance resistance was compensated via bridge balance for current clamp recordings.

6.2.5 Statistics and analysis

Python and GraphPad were used to run statistical analyses. Two-tailed unpaired t-tests were used for comparing between groups for both passive and spike parameters. Significant p-values are shown in the figure caption where appropriate. A two-way ANOVA test with Sidak's multiple comparisons was used to compare the mean firing frequency across current injections. P-values from the two-way ANOVA are summarized in Table 6.2, with the results of the multiple comparisons in Table 6.3 and Table 6.4. Cells with passive properties with z-scores greater than 3 were considered outliers and excluded from the analysis. Box

plots show the mean as the center line, with the box representing the data quartiles (25% and 75%), and the whiskers representing 1.5*IQR (interquartile range) away from the quartiles.

6.3 Results

6.3.1 Entorhinal Cortex

Parvalbumin Interneurons

We were interested in intrinsic properties of PV interneurons in the entorhinal cortex (Figure 6.2A-B)to determine whether the App^{SAA} model shows any indication of altered excitability. As we hypothesized, changes in firing rate indicate significant hypoexcitablity across nearly all current injections (Figure 6.2C). The passive properties of these cells showed no significant differences (Figure 6.2D). However, the active properties did show increased action potential half-width and decreased maximum dV/dt (Figure 6.2E) in the App^{SAA} mice.

Excitatory Neurons

We also considered the intrinsic properties of excitatory neurons in the entorhinal cortex (Figure 6.3A) to determine if there may be a corresponding change in excitability. The two-way ANOVA test did not yield a significant result, however, the post-hoc test indicated that these cells were hyperexcitable near threshold (Figure 6.3B-C). The membrane capacitance and tau were both decreased in App^{SAA} (Figure 6.3D). These cells also exhibited decreased action potential half-width (Figure 6.3E) in the App^{SAA} mice.

6.3.2 Medial Prefrontal Cortex

Anterior Cingulate Cortex

There were no significant changes in firing frequency or passive or active properties in PV cells in the ACC (Figure 6.4). The excitatory neurons also did not show statistically

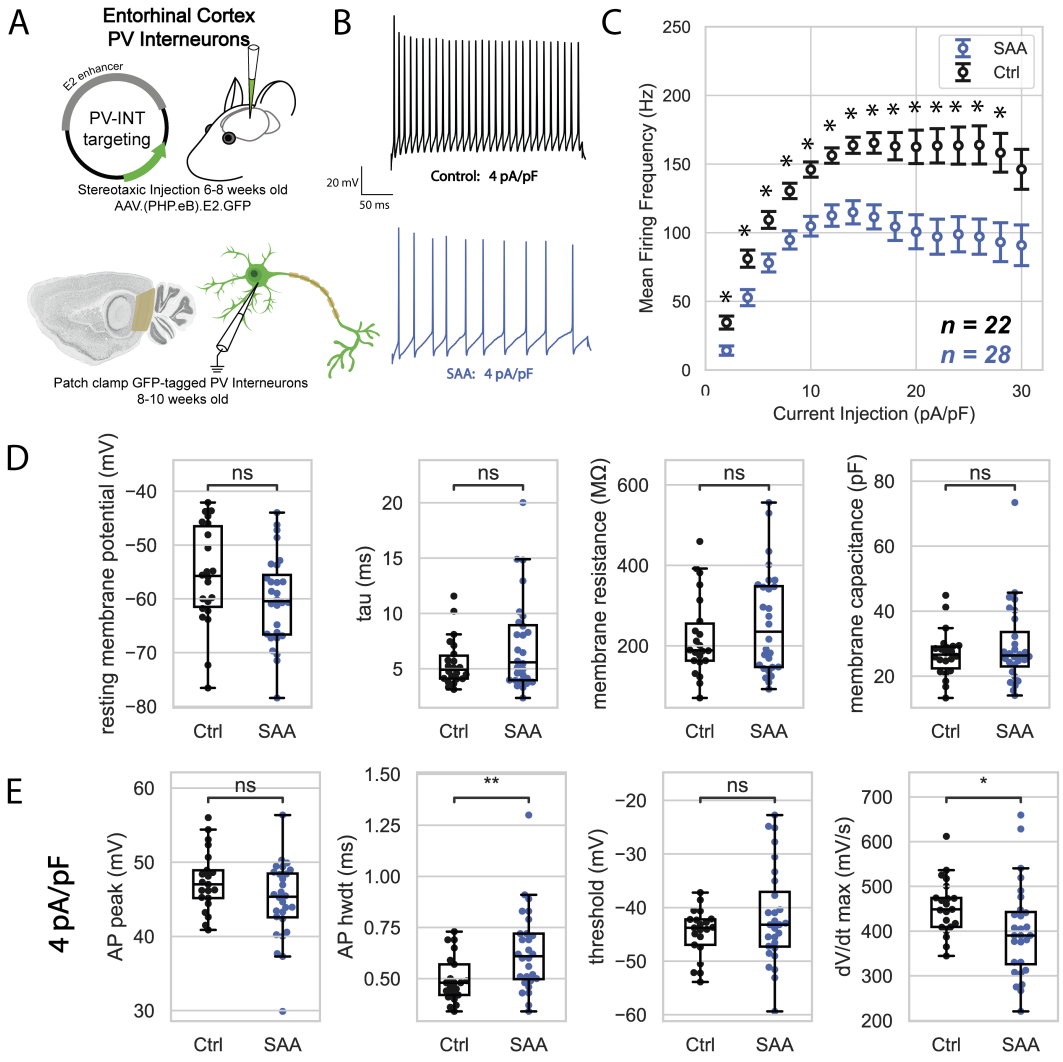

Figure 6.2: A. Schematic of the experimental approach, including injection of the AAV in the entorhinal cortex and patch clamp fluorescent PV interneurons. B. Representative current clamp traces from the AD model (SAA, blue) and the corresponding control (Ctrl, black) in response to a 4 pA/pF current injection. C. Summary of mean firing frequency as a function of current injection. SAA exhibits significant hypoexcitability across all current injections (Sidak's multiple comparison's test, * indicates $p < 0.05$). (Ctrl n = 22 cells from 4 mice, SAA n = 28 cells from 3 mice) D. Passive properties of PV interneurons: resting membrane potential, time constant (τ), membrane resistance, and membrane capacitance. E. Properties of the first action potential evoked from a 4 pA/pF current injection (from left to right): action potential peak, action potential half-width, threshold, and maximum dV/dt. Action potential half-width is significantly increased in SAA (unpaired t-test p = 0.0073) and maximum dV/dt is decreased (unpaired t-test p = 0.043).

significant changes in excitability in the ACC (Figure 6.5), however there were evident changes in some passive properties and notably in action potential half-width.

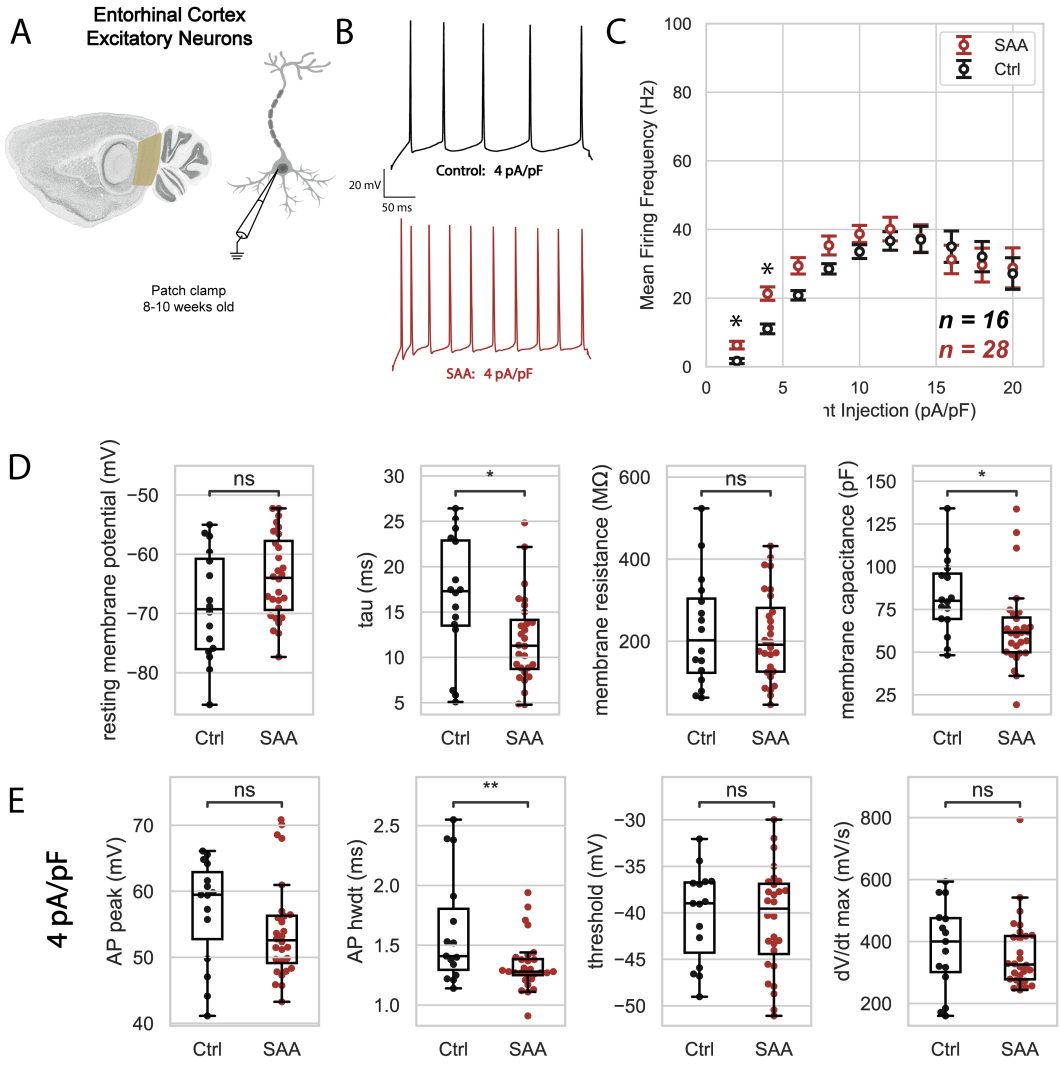

Figure 6.3: A. Schematic of the experimental approach: patch clamp excitatory neurons. B. Representative current clamp traces from the AD model (SAA, blue) and the corresponding control (Ctrl, black) in response to a 4 pA/pF current injection. C. Summary of mean firing frequency as a function of current injection. SAA exhibits slight hyperexcitability near threshold (Sidak's multiple comparison's test, * indicates $p < 0.05$). (Ctrl n = 16 cells from 3 mice, SAA n = 28 cells from 3 mice) D. Passive properties of PV interneurons: resting membrane potential, time constant (τ), membrane resistance, and membrane capacitance. Tau is significantly decreased in SAA (unpaired t-test p = 0.010). Membrane capacitance is decreased in SAA (unpaired t-test p = 0.015). E. Properties of the first action potential evoked from a 4 pA/pF current injection (from left to right): action potential peak, action potential half-width, threshold, and maximum dV/dt. Action potential half-width is significantly decreased in SAA (unpaired t-test p = 0.0094).

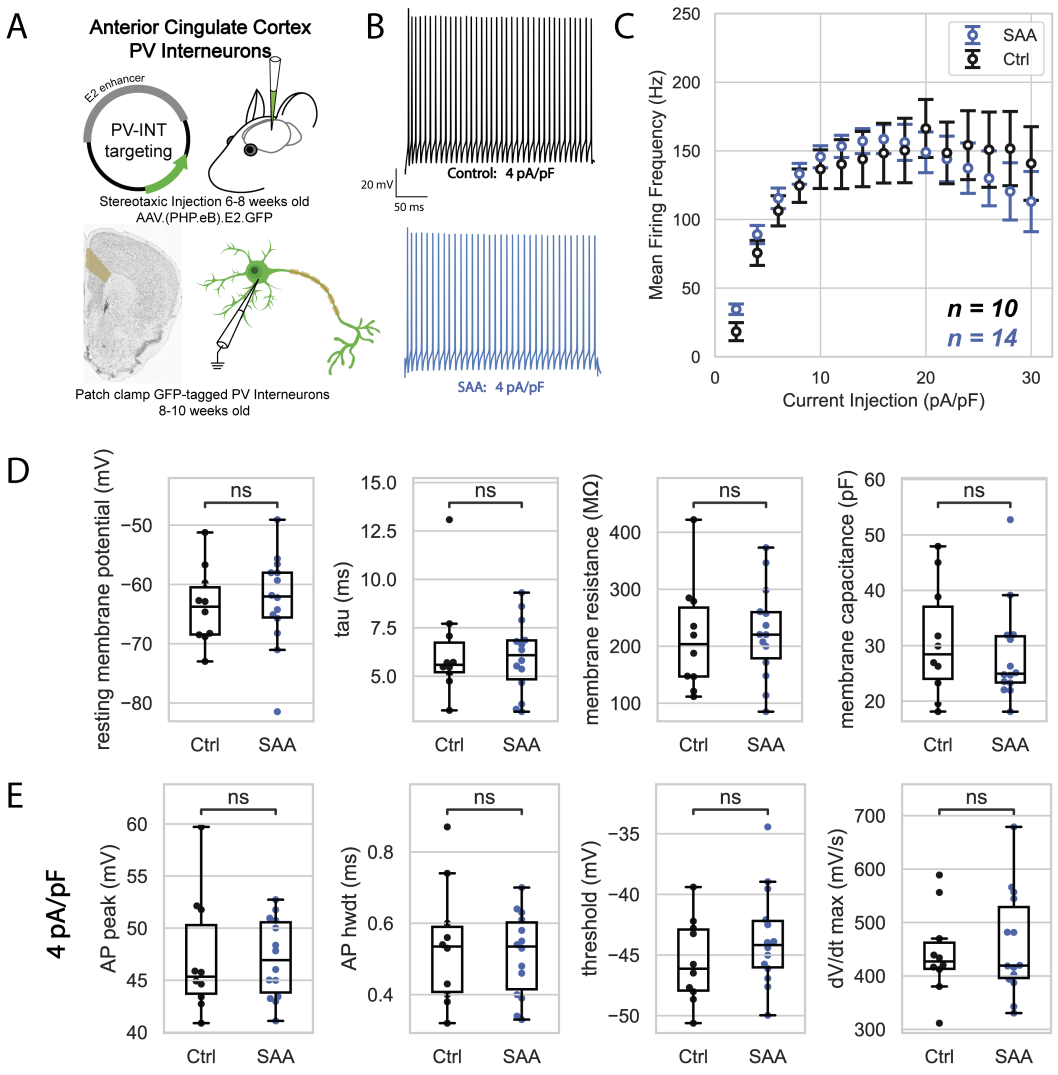

Figure 6.4: A. Schematic of the experimental approach, including injection of the AAV in the medial prefrontal cortex and patch clamp fluorescent PV interneurons. B. Representative current clamp traces from the AD model (SAA, blue) and the corresponding control (Ctrl, black) in response to a 4 pA/pF current injection. C. Summary of mean firing frequency as a function of current injection, with no significant difference in firing frequency across current injections. (Ctrl n = 10 cells from 3 mice, SAA n = 14 cells from 4 mice) D. Passive properties of PV interneurons: resting membrane potential, time constant (τ), membrane resistance, and membrane capacitance. E. Properties of the first action potential evoked from a 4 pA/pF current injection (from left to right): action potential peak, action potential half-width, threshold, and maximum dV/dt.

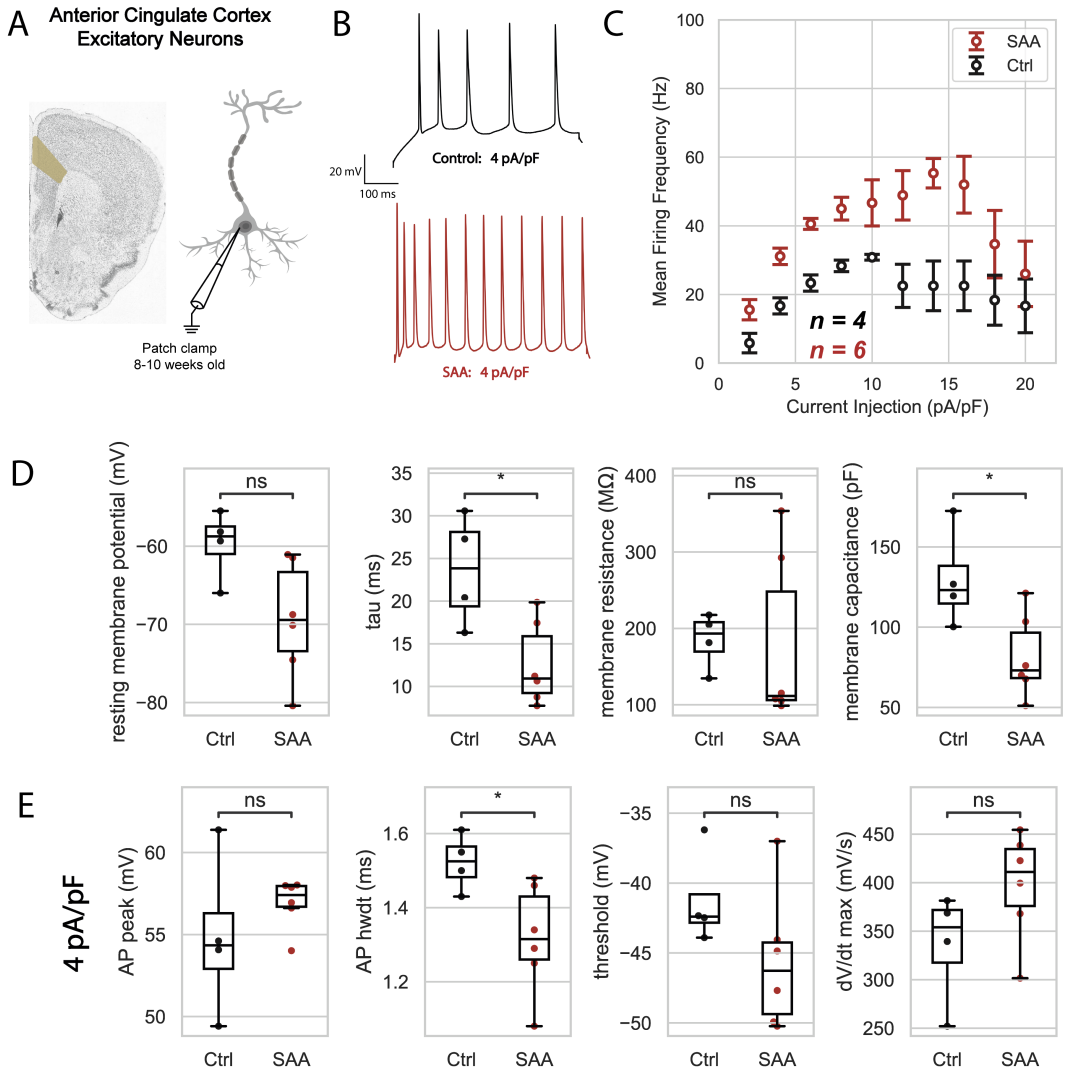

Figure 6.5: A. Schematic of the experimental approach: patch clamp excitatory neurons in the anterior cingulate cortex. B. Representative current clamp traces from the AD model (SAA, blue) and the corresponding control (Ctrl, black) in response to a 4 pA/pF current injection. C. Summary of mean firing frequency as a function of current injection. (Ctrl n = 4 cells from 1 mice, SAA n = 6 cells from 1 mice) D. Passive properties of excitatory neurons: resting membrane potential, time constant (τ), membrane resistance, and membrane capacitance. Tau is decreased in SAA (unpaired t-test p = 0.015). Membrane capacitance is decreased in SAA (unpaired t-test p = 0.027). E. Properties of the first action potential evoked from a 4 pA/pF current injection (from left to right): action potential peak, action potential half-width, threshold, and maximum dV/dt. Action potential half-width is decreased in SAA (unpaired t-test p = 0.034).

Prelimbic Cortex

In the PL (Figure 6.6A-C), the firing frequency was affected by strain and current injection. The multiple comparisons test did not yield any particular current injection as significant. Interestingly, the resting membrane potential, tau, and membrane resistance of these cells were all significantly increased in App^{SAA} (Figure 6.6D). Furthermore, the action potential half width was also increased (Figure 6.6E).

Infralimbic Cortex

In the IL (Figure 6.7A-C), the firing frequency was similarly affected by strain and current injection. The multiple comparisons test did not yield any particular current injection as significant. No differences in passive (Figure 6.7D) or active properties was observed (Figure 6.7E) in this region.

6.3.3 Primary Visual Cortex

Parvalbumin Interneurons

To determine whether PV interneuron hypoexcitability emerged as a function of brain region or if it is a brain-wide phenomenon, we recorded from PV interneurons and excitatory neurons in regions which are not typically implicated in early AD. First we looked at the primary visual cortex (Figure 6.8A).The visual cortex did not show indications of altered excitability (Figure 6.8B-C) or differences in passive properties(Figure 6.8D). However, there were increased action potential properties, such as action potential peak and dV/dt max (Figure 6.8E).

Excitatory Neurons

In terms of the excitatory neurons (Figure 6.9A), there were no differences in firing frequency (Figure 6.9B-C) in primary visual cortex (V1). There was a difference in resting

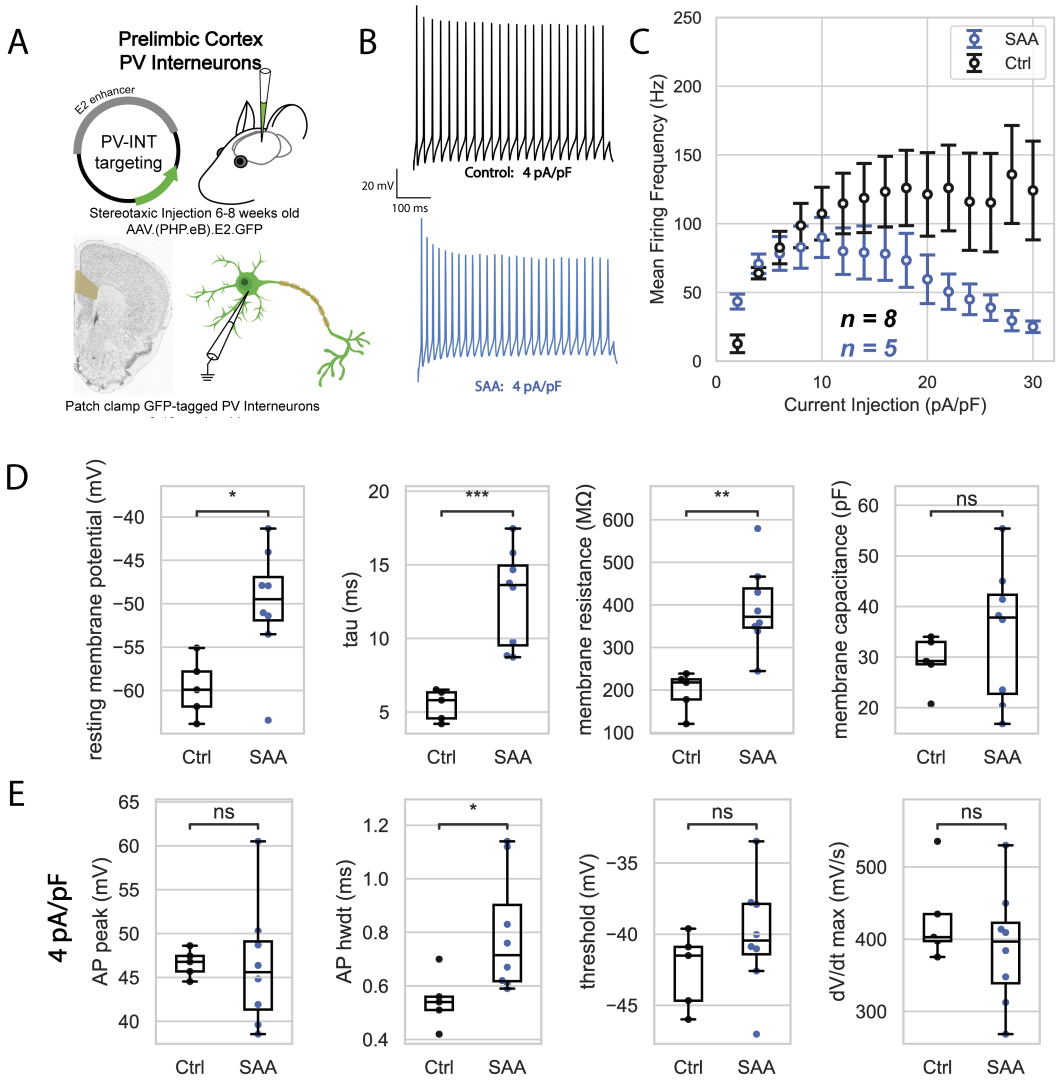

Figure 6.6: A. Schematic of the experimental approach, including injection of the AAV in the medial prefrontal cortex and patch clamp fluorescent PV interneurons. B. Representative current clamp traces from the AD model (SAA, blue) and the corresponding control (Ctrl, black) in response to a 4 pA/pF current injection. C. Summary of mean firing frequency as a function of current injection, with slight hypoexcitability in SAA. (Ctrl n = 8 cells from 2 mice, SAA n = 5 cells from 2 mice) D. Passive properties of PV interneurons: resting membrane potential, time constant (τ), membrane resistance, and membrane capacitance. Resting membrane potential (unpaired t-test p = 0.013), tau (unpaired t-test p = 0.00063), and membrane resistance (unpaired t-test p = 0.0017) are significantly increased in SAA. E. Properties of the first action potential evoked from a 4 pA/pF current injection (from left to right): action potential peak, action potential half-width, threshold, and maximum dV/dt. Action potential half-width is increased in App^{SAA} (unpaired t-test p = 0.042).

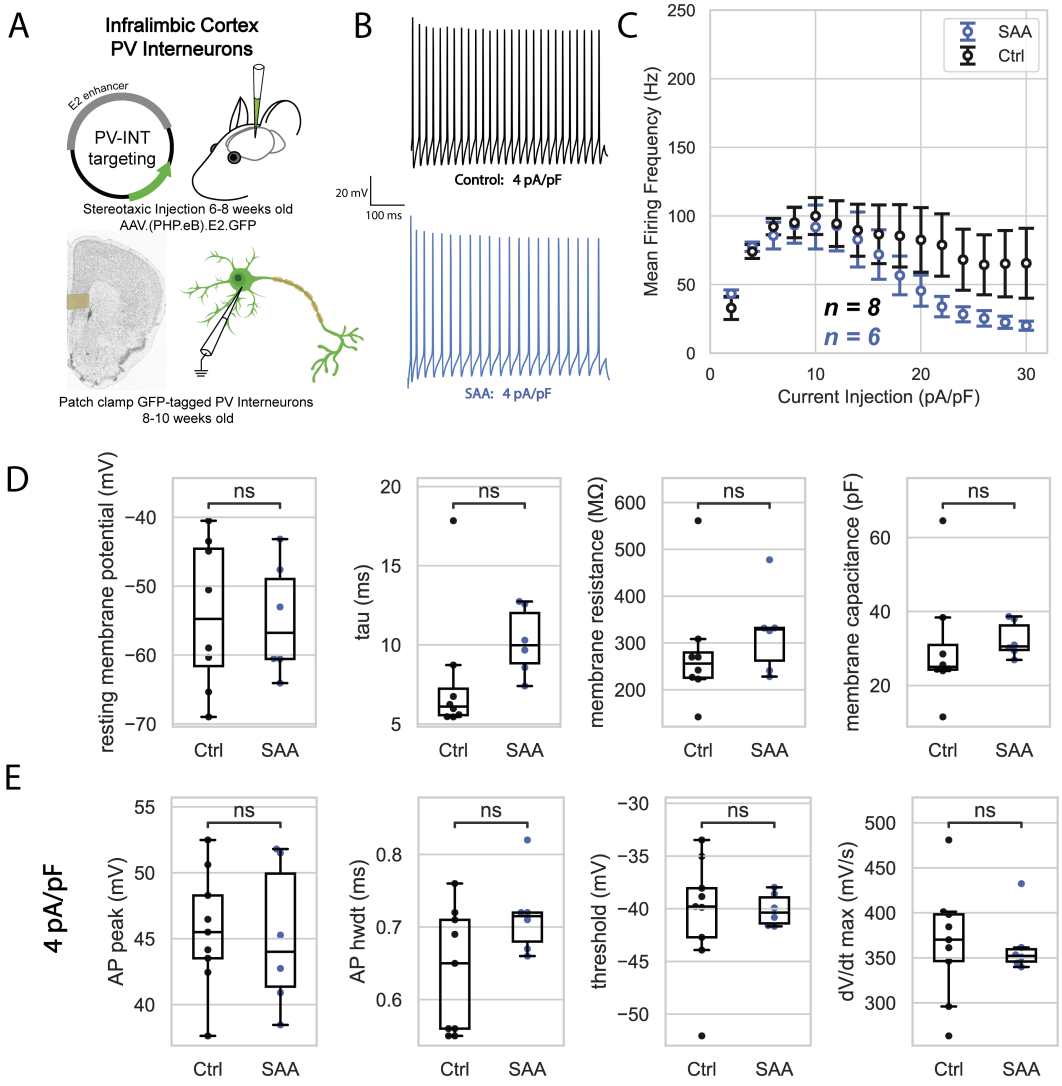

Figure 6.7: A. Schematic of the experimental approach, including injection of the AAV in the medial prefrontal cortex and patch clamp fluorescent PV interneurons. B. Representative current clamp traces from the AD model (SAA, blue) and the corresponding control (Ctrl, black) in response to a 4 pA/pF current injection. C. Summary of mean firing frequency as a function of current injection, with slight hypoexcitability in SAA. (Ctrl n = 8 cells from 3 mice, SAA n = 6 cells from 2 mice) D. Passive properties of PV interneurons: resting membrane potential, time constant (τ), membrane resistance, and membrane capacitance. E. Properties of the first action potential evoked from a 4 pA/pF current injection (from left to right): action potential peak, action potential half-width, threshold, and maximum dV/dt.

membrane potential, with App^{SAA} exhibiting a slightly lower average (Figure 6.9D). As expected, there were no changes in action potential properties (Figure 6.9E).

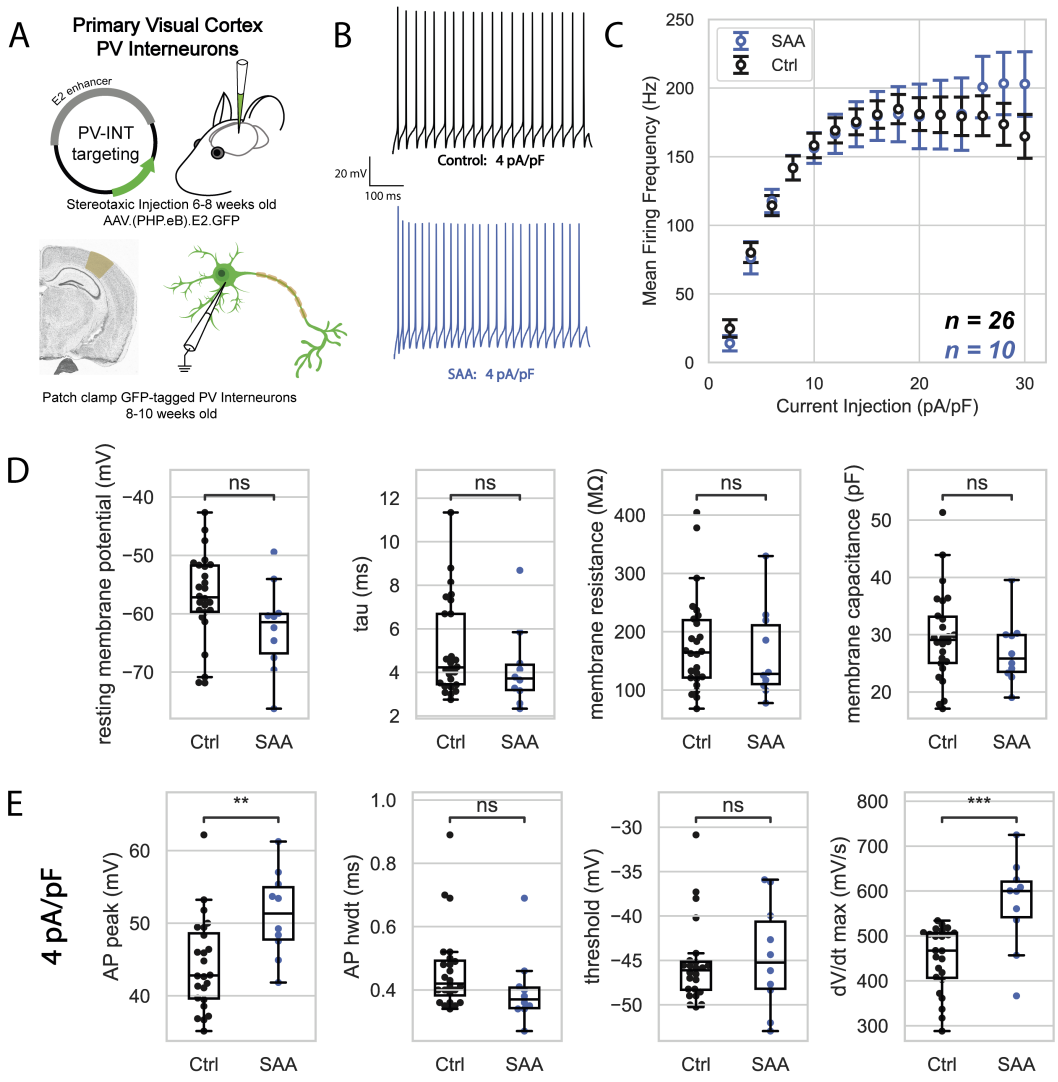

Figure 6.8: A. Schematic of the experimental approach, including injection of the AAV in the primary visual cortex and patch clamp fluorescent PV interneurons. B. Representative current clamp traces from the AD model (SAA, blue) and the corresponding control (Ctrl, black) in response to a 4 pA/pF current injection. C. Summary of mean firing frequency as a function of current injection, with no significant difference in firing frequency. (Ctrl n = 26 cells from 3 mice, SAA n = 10 cells from 3 mice) D. Passive properties of PV interneurons: resting membrane potential, time constant (τ), membrane resistance, and membrane capacitance. E. Properties of the first action potential evoked from a 4 pA/pF current injection (from left to right): action potential peak, action potential half-width, threshold, and maximum dV/dt. Action potential peak (unpaired t-test p = 0.0056) and maximum dV/dt are increased in App^{SAA} (unpaired t-test p = 0.00032)).

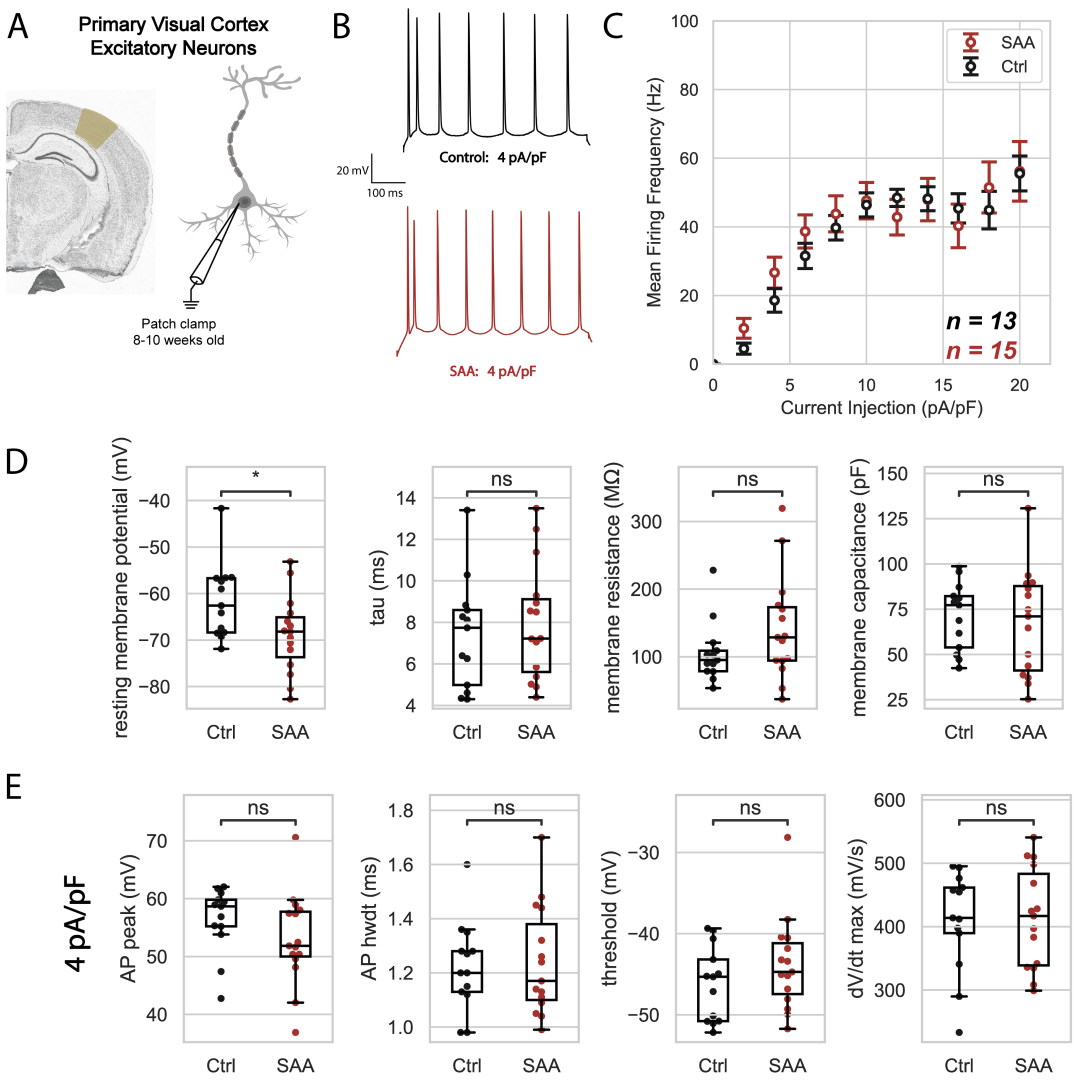

Figure 6.9: A. Schematic of the experimental approach: patch clamp excitatory neurons. B. Representative current clamp traces from the AD model (SAA, blue) and the corresponding control (Ctrl, black) in response to a 4 pA/pF current injection. C. Summary of mean firing frequency as a function of current injection, with no differences in firing frequency. (Ctrl n = 13 cells from 2 mice, SAA n = 15 cells from 3 mice) D. Passive properties of excitatory neurons: resting membrane potential, time constant (τ), membrane resistance, and membrane capacitance. Resting membrane potential is slightly decreased in SAA (unpaired t-test p = 0.027). E. Properties of the first action potential evoked from a 4 pA/pF current injection (from left to right): action potential peak, action potential half-width, threshold, and maximum dV/dt.

6.3.4 Secondary Motor Cortex

Parvalbumin Interneurons

We also recorded from the secondary motor cortex (M2), which is adjacent to the mPFC. Unsurprisingly, there were no differences in intrinsic properties of the PV interneurons in this brain region (Figure 6.10).

Excitatory Neurons

In secondary motor cortex (M2), the excitatory neurons exhibited hyperexcitability in App^{SAA} in response to higher current injections (Figure 6.11A-C). We did not observe any significant changes in passive or active properties in this region (Figure 6.11D-E).

Statistics

Table 6.2: Two-way ANOVA Results, by brain region

	EC	**ACC (mPFC)**	**PL (mPFC)**	**IL (mPFC)**	**V1**	**M2**
PV Interneurons	0.029	0.29	$<$0.0001	0.0066	0.38	0.73
Excitatory Neurons	0.58	0.40	NA	NA	0.78	$<$0.0001

6.4 Discussion

Here we systematically studied the intrinsic properties of parvalbumin interneurons and excitatory neurons in an App^{SAA} mouse model of Alzheimer's disease. We sought to quantify whether PV interneurons exhibit hypoexcitability in this mouse model of AD, as a potential contributor to the hyperexcitability that is apparent in early AD [34, 36, 35]. As hypothesized, we found that PV interneurons do exhibit hypoexcitability across the entorhinal cortex as well as subregions in the medial prefrontal cortex. Similarly, we found that there was no change in PV interneuron excitability in the visual or motor cortices.

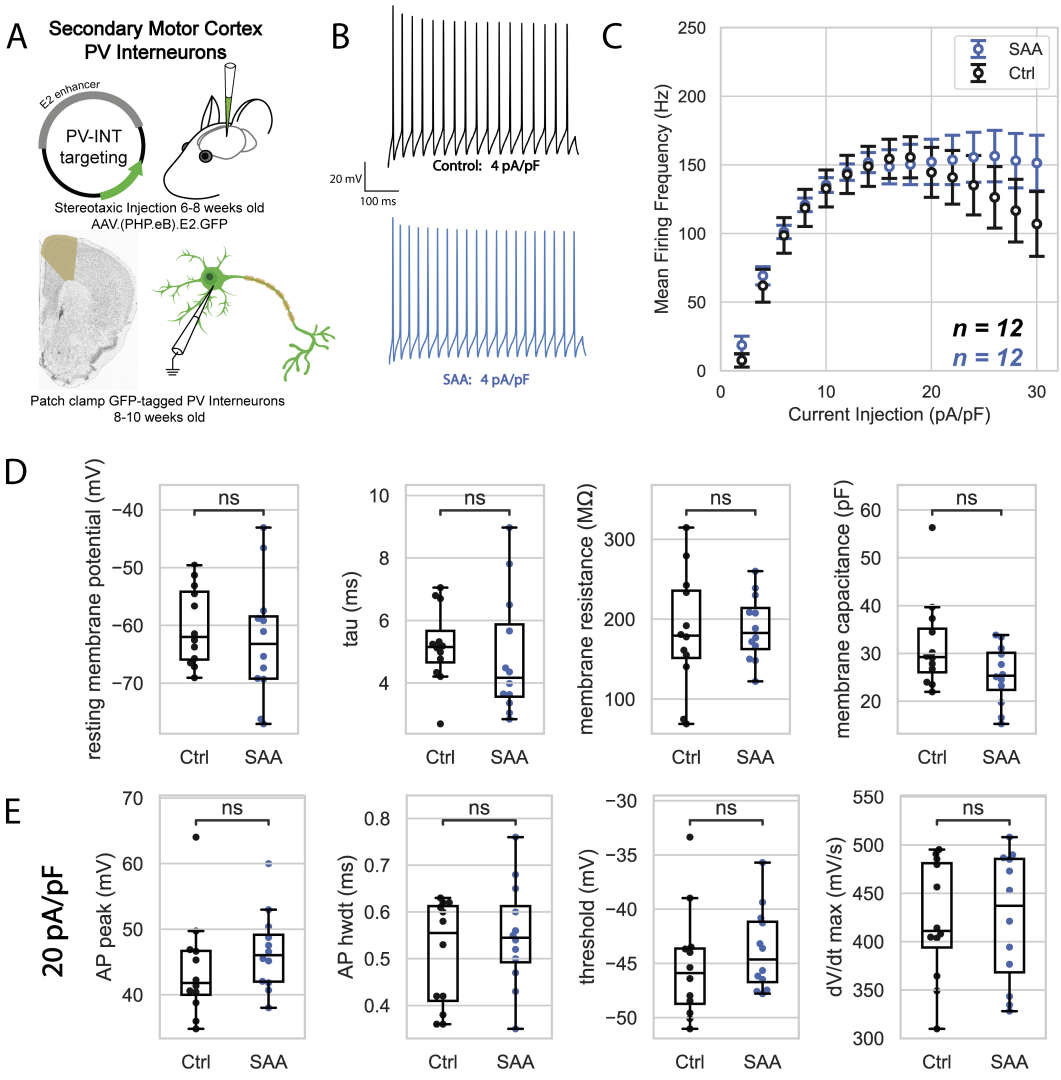

Figure 6.10: A. Schematic of the experimental approach, including injection of the AAV in the secondary motor cortex and patch clamp fluorescent PV interneurons. B. Representative current clamp traces from the AD model (SAA, blue) and the corresponding control (Ctrl, black) in response to a 4 pA/pF current injection. C. Summary of mean firing frequency as a function of current injection, with no significant difference in firing frequency. (Ctrl n = 12 cells from 2 mice, SAA n = 12 cells from 3 mice) D. Passive properties of PV interneurons: resting membrane potential, time constant (τ), membrane resistance, and membrane capacitance. E. Properties of the first action potential evoked from a 20 pA/pF current injection (from left to right): action potential peak, action potential half-width, threshold, and maximum dV/dt.

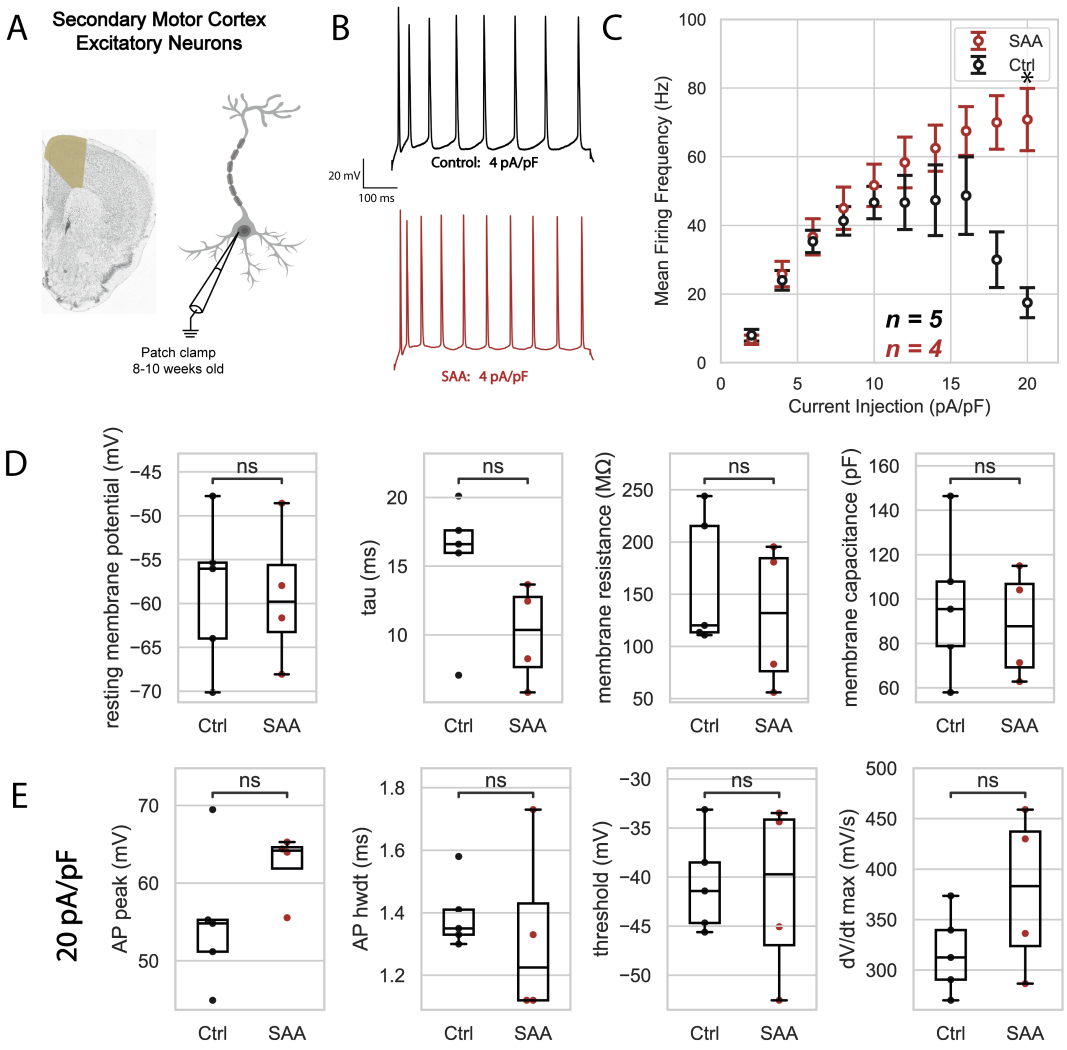

Figure 6.11: A. Schematic of the experimental approach: patch clamp excitatory neurons in the secondary motor cortex. B. Representative current clamp traces from the AD model (SAA, blue) and the corresponding control (Ctrl, black) in response to a 4 pA/pF current injection. C. Summary of mean firing frequency as a function of current injection, with significant differences in firing frequency (two-way ANOVA $p < 0.0001$). (Ctrl n = 5 cells from 2 mice, SAA n = 4 cells from 2 mice) D. Passive properties of excitatory neurons: resting membrane potential, time constant (τ), membrane resistance, and membrane capacitance. E. Properties of the first action potential evoked from a 20 pA/pF current injection (from left to right): action potential peak, action potential half-width, threshold, and maximum dV/dt.

6.4.1 Entorhinal Cortex

The hypoexcitability found in the entorhinal cortex aligns with the initial hypothesis, supporting the idea that PV cells in this region are affected by early disease progression. Ex-

Table 6.3: Sidak's multiple comparison p-values, by region and current injection for PV interneurons

Current Injection (pA/pF)	EC	ACC (mPFC)	PL (mPFC)	IL (mPFC)	V1	M2
2	0.010	0.52	0.055	0.92	0.97	0.97
4	0.013	0.98	>0.99	>0.99	>0.99	>0.99
6	0.0070	>0.99	>0.99	>0.99	>0.99	>0.99
8	0.0009	>0.99	0.99	>0.99	>0.99	>0.99
10	0.0002	>0.99	0.98	>0.99	>0.99	>0.99
12	0.0003	>0.99	0.85	>0.99	>0.99	>0.99
14	0.0001	>0.99	0.85	>0.99	>0.99	>0.99
16	0.0001	>0.99	0.881	>0.99	>0.99	>0.99
18	0.0009	>0.99	0.82	0.82	>0.99	>0.99
20	0.0058	>0.99	0.77	0.55	>0.99	>0.99
22	0.0048	>0.99	0.59	0.27	>0.99	>0.99
24	0.010	>0.99	0.78	0.36	>0.99	>0.99
26	0.011	>0.99	0.74	0.86	>0.99	>0.99
28	0.025	>0.99	0.55	0.51	0.99	0.99
30	0.11	0.99	0.65	0.51	0.96	0.99

Table 6.4: Two-way ANOVA p-values by region for excitatory neurons

Current Injection (pA/pF)	EC	ACC (mPFC)	V1	M2
2	0.0093	0.65	0.63	0.99
4	0.0025	0.48	0.86	>0.99
6	0.084	0.46	0.95	>0.99
8	0.49	0.68	0.99	>0.99
10	0.87	0.91	>0.99	0.99
12	0.99	0.50	0.98	0.97
14	>0.99	0.34	>0.99	0.95
16	>0.99	0.55	0.99	0.89
18	>0.99	0.95	0.99	0.090
20	>0.99	0.99	>0.99	0.047

actly the mechanism in play is not fully clear, however the resolution of the data shown here is laying the foundation towards a full understanding these cell types at the molecular level. Specifically, the increased half-width of the action potentials in the App^{SAA} mice suggests differences in ion channel function or density, in particular voltage gated sodium and potassium channels [44, 134]. Together with the decreased maximum dV/dt, sodium channels are more likely involved. Additionally, while passive properties showed no sig-

nificant differences, it is essential to consider that subtle changes in membrane properties may still impact neuronal excitability through mechanisms such as shunting inhibition or altered integration of synaptic inputs [135, 136].

We found increased firing of excitatory neurons near threshold, however firing rate was unaffected at higher current injections. This result supports the idea that there may a lack of inhibitory neurotransmission to these excitatory neurons [137], however post-synaptic current data should be collected to validate this hypothesis. Notably, the time constant and membrane capacitance is decreased in this App^{SAA} model, which may explain the hyperexcitability of these cells since lower time constant results in faster cell responses. These passive changes, together with the decreased half-width of the action potentials, suggest that both the size of these excitatory neurons and the ion channel activity on these neurons may contribute to the cells' hyperexcitability. Since smaller excitatory neurons can respond to inputs faster, circuit hyperexcitability may be a result of a combination of structural changes in these cells.

Recent evidence has shown that both PV interneurons [44, 59, 138, 129] and excitatory neurons [128] are vulnerable in AD. This work supports the idea that there is reduced excitability of PV interneurons in early AD, specifically in the entorhinal cortex, which may contribute to circuit hyperexcitability. Future work could include looking at the ratios of excitatory to inhibitory post synaptic currents to determine whether this reduced inhibition is truly affecting the excitatory neurons. The evidence across multiple models of AD supports the overarching hypothesis that PV cells in the entorhinal cortex (EC) are particularly vulnerable and interesting early therapeutic targets.

6.4.2 Medial Prefrontal Cortex

The original intent of studying the medial prefrontal cortex was to collect and compare data from the App^{SAA} model and control across the entire region. Surprisingly, when the data was analyzed by sub-region, mild patterns of hypoexcitability emerged albeit with lower

statistical significance due to a divided sample size.

In a healthy brain, the hippocampus typically provides the majority of inputs to the PL and IL, but not the ACC [130]. Similarly, we found no indications of altered excitability of PV interneurons in the anterior cingulate cortex, in firing rate or active or passive properties. Furthermore, the IL and PL in particular play important roles in working memory and spatial memory [139, 140, 141]. Since these sub-regions are important for working memory, they are likely vulnerable even in early AD. Supporting this idea, we found that the prelimbic and infralimbic cortices did display hypoexcitability. Since the two-way ANOVA yielded a significant result in these two regions, we can conclude that, together, current injection and strain have an effect on firing rate. However, because the post-hoc test did not indicate which groups are statistically different, more data should be collected to determine the magnitude of altered excitability in these regions.

The increased membrane resistance, which results in increased time constant, of the PV interneurons in the PL indicates that the cells in the App^{SAA} model are slower to respond to stimuli and thus cannot fire at their maximum rate compared to the control.

While the PL exhibited significant changes in intrinsic properties of PV interneurons, the IL showed no differences in passive or active properties. This suggests even between the PL and IL there are functional differences in these cells that both result in hypoexcitability of these PV interneurons.

While there have been several studies addressing the role of PV interneurons in the mPFC [142, 143], there is little known about their role in AD. One study showed that mPFC PV interneurons are more sparse as well as hypoexcitable in an APP model [144] compared to the control. This work together with this early study in the mPFC supports the idea that PV interneurons play an important role in early AD progression, specifically in the mPFC. In addition, the mPFC pyramidal neurons were hyperexcitable in the 3xTg mouse model of AD [132], which aligns with the trends we see in the excitatory neurons. This further provides a foundation to study the regional emergence of altered excitability,

in both PV and excitatory neurons.

6.4.3 Primary Visual Cortex

Typically, V1 is not commonly studied in early AD since it does not play a major role in memory and cognition. However, V1 is affected in late disease progression, as amyloid and tau are often accumulated across the entire cortex, and visual and motor systems are severely affected in later stage AD [145]. Here we sought to determine whether PV and excitatory neurons were affected in early AD.

Our data showed no indication of altered excitability of PV interneurons via firing frequency or passive membrane properties. Interestingly, the App^{SAA} mice showed increased action potential peak and maximum dV/dt. These two metrics often indicate modifications in sodium ion channel activity [134]. It is possible these changes in action potential metrics precede changes in excitability that may occur later in disease progression, though additional studies would be required to support this claim. Similarly, as hypothesized, there was no apparent change in excitability of excitatory neurons in V1, aside from slight differences in resting membrane potential.

6.4.4 Secondary Motor Cortex

The secondary motor cortex, located adjacent to the medial prefrontal cortex, is also a region which was hypothesized to exhibit little to no differences in PV interneuron activity in early AD. We found no changes in PV interneuron activity, but did find hyperexcitability in excitatory neurons. Interestingly, the motor cortex in general has been shown to be disinhibited [146] and hyperexcitable [147, 148] in human AD patients. Furthermore, there is some evidence of alterations in the primary motor cortex in intermediate time points of disease progression [149] in 3xTg mice. Thus, the hyperexcitability of the excitatory neurons in the motor cortex is likely unrelated to the balance of inhibition provided by the PV interneurons. Alternatively, this increased excitability may be due to increased

presynaptic glutamate release or potentially inhibition from other inhibitory cell types, such as somatostatin interneurons.

6.5 Conclusions

In this systematic study of PV interneurons and excitatory neurons, we found that PV interneurons exhibit severe hypoexcitability in the entorhinal cortex and mild hypoexcitability in the medial prefrontal cortex, but not across other cortical brain regions such as the visual or motor cortices. This is likely due to differences in voltage gated sodium or potassium channels. The excitatory neurons in the entorhinal cortex exhibited mild hyperexcitability, hypothesized due to reduced inhibition. This work did not record excitatory and inhibitory post-synaptic currents, which would show whether changes in inhibitory cell excitability affect excitatory neuron excitability. Thus, we cannot conclude that lack of inhibition is the direct cause of hyperexcitability. However, we predict that if future studies do address this, there would be reduced E/I ratio in excitatory neurons.

There were several other limitations to this study. For one, we recorded from cells in four major brain regions, however there are many brain regions which would be interesting to address as well, such as the hippocampus or the amygdala. All of the data shared here was collected at one early time point in disease progression, at two months of age, and it is important to understand how these cells change over time as well. Thus, performing similar experiments in the same regions at 4 months and at 8 months of age would provide insight into whether this hypoexcitability persists or is balanced later in the disease, especially when plaques begin to accumulate. We also only studied a single mouse model of AD, and it would be valuable to learn whether PV cells are affected similarly across familial and sporadic models.

This body of work is evidence of the role of PV interneurons in AD, suggesting that these cells are interesting therapeutic targets for early AD intervention. Specifically, targeting voltage-gated sodium channels in PV interneurons in the entorhinal cortex is a promis-

ing direction for future work towards finding effective therapies for this neurodegenerative disease.

CHAPTER 7
CONCLUSION

7.1 Major Contributions

This thesis has made significant strides in addressing key challenges in neuroscience research through a multifaceted approach. Firstly, our development of an automated pipette positioning correction system has improved the automated patch clamp electrophysiology state-of-the-art by mitigating positioning errors during experiments, thereby enhancing the accuracy and success rates of whole-cell recordings. We have advanced the capabilities of automated patch clamp experiments, improving the accuracy, efficiency, and success rates of recordings. These advancements not only streamline experimental procedures but also reduce the burden on researchers, allowing for more time and resources to be allocated towards data analysis and interpretation.

Secondly, the novel integration of differential interference microscopy with a convolutional neural network has facilitated the automated detection of healthy neurons in acute brain tissue slices in real time, streamlining the process and reducing the expertise required for cell selection in patch clamp experiments. Our exploration of the patch-walking technique has demonstrated its efficacy in efficiently probing synaptic connections, offering a promising alternative to traditional methods and enabling a more comprehensive understanding of neuronal circuitry. This integration of automation and efficiency-enhancing techniques opens up possibilities for scaling up experiments, facilitating large-scale studies and accelerating progress in our understanding of neural circuitry and function.

Lastly, our investigation into interneuron dysfunction in Alzheimer's Disease represents a crucial step towards discovering the underlying mechanisms of this complex neurodegenerative disorder, shedding light on the regional emergence of interneuron dysregulation and

its implications for circuit function. Together, these findings not only help advance our understanding of fundamental neuroscience but also hold significant promise for informing future research endeavors and therapeutic interventions aimed at addressing neurological disorders.

7.2 Future Work

7.2.1 Automated patch clamp

In general, the future of automated patch clamp is likely to be more limited by the biology than the automation itself. In my experience, the patcherBot is best used for cultured cells and brain slices from young mice. Studying cell type-specific properties in aged mice (6 months or older) with high yield has been a challenge in the field for years, and would enable the same type of systematic studies I have done here in neurodegenerative diseases. Finding the key to high success rates in aged mice, and even more so making that process automatic, would be revolutionary in the field of electrophysiology.

As far as other improvements to the current state-of-the-art, the pipette correction algorithm has its limitations with regards to the experimental set up, so expanding the training data set to include different objectives and different manipulator angles could improve how generalizable the tool is across different patch clamp setups. The neuron detection can be expanded to identify different types of cells, as well as adding segmentation and real-time tracking. In particular, cell type-specific classification could change the way the field identifies cell types in brain slices, potentially eliminating the need for viral injections and fluorescent labeling.

7.2.2 Parvalbumin interneurons in Alzheimer's disease

While this work has laid some groundwork and offered some insights into the role of PV interneurons in AD, there are several interesting directions that the project could go moving forward. At a high level, the project could investigate these cells in a more broad sense or

go deeper into the work that has begun already. In terms of going broader, there are a handful of subtle changes that would produce entirely new datasets:

- Keep the brain regions and strain the same and change the time point in disease progression (perhaps 6 and 12 months of age) could reveal if these PV cells maintain altered excitability or if there are compensatory mechanisms that balance the circuit.
- Keep the brain regions and time point the same and change the strain of interest. This type of study would indicate whether the excitability of these cells is potentially an artifact of a genetic mutation (only familial AD) or if it remains true for sporadic models as well.
- Keep the strain and time point the same and change the brain regions. This direction in particular would directly build upon the work done here to discern what other regions are vulnerable in early AD. For instance, looking at the hippocampus and the amygdala could be of interest considering their role in memory.

The project could also use the findings in this work to take the study a step further and look closer into mechanistically what may be happening:

- In the entorhinal cortex, look at the behavior of PV interneurons in different layers or different sub-regions such as the lateral entorhinal cortex or medial entorhinal cortex. Furthermore, based on the potential role of sodium channels, investigating what may happen when these channels are blocked by an antagonist could provide more insights into the mechanism behind the hypoexcitability.
- In the medial prefrontal cortex, collecting more data in the prelimbic and infralimbic cortices would make it more clear how the PV cells differ in the App^{SAA} model.
- Simultaneous recordings from both PV and connected excitatory neurons would provide insight into the direct effect of hypoexcitability onto synaptic transmission

REFERENCES

[1] S. Herculano-Houzel, "The human brain in numbers: A linearly scaled-up primate brain," *Frontiers in Human Neuroscience*, vol. 3, Nov. 2009.

[2] E. R. Kandel, 4th ed. New York, NY: McGraw-Hill Health Professions Division, 2000.

[3] P. E. Ludwig, V. Reddy, and M. Varacallo, "Neuroanatomy, central nervous system (cns)," 2022.

[4] M. Hoffmann, "The human frontal lobes and frontal network systems: An evolutionary, clinical, and treatment perspective," *ISRN Neurology*, vol. 2013, pp. 1–34, Mar. 2013.

[5] M. A. Hofman, "Evolution of the human brain: When bigger is better," *Frontiers in Neuroanatomy*, vol. 8, Mar. 2014.

[6] R. T. Narayanan *et al.*, "Beyond columnar organization: Cell type-and target layer-specific principles of horizontal axon projection patterns in rat vibrissal cortex," *Cerebral cortex*, vol. 25, no. 11, pp. 4450–4468, 2015.

[7] P. Verma, A. Kienle, D. Flockerzi, and D. Ramkrishna, "Using bifurcation theory for exploring pain," *Industrial & Engineering Chemistry Research*, vol. 59, no. 6, pp. 2524–2535, 2019.

[8] R. N. Lamptey, B. Chaulagain, R. Trivedi, A. Gothwal, B. Layek, and J. Singh, "A review of the common neurodegenerative disorders: Current therapeutic approaches and the potential role of nanotherapeutics," *International Journal of Molecular Sciences*, vol. 23, 3 Feb. 2022.

[9] Z. Breijyeh and R. Karaman, "Comprehensive review on alzheimer's disease: Causes and treatment," *Molecules*, vol. 25, 24 Dec. 2020.

[10] M. E. Belloy, V. Napolioni, and M. D. Greicius, "A quarter century of apoe and alzheimer's disease: Progress to date and the path forward," *Neuron*, vol. 101, pp. 820–838, 5 2019.

[11] D. S. Knopman *et al.*, "Alzheimer disease," *Nature Reviews Disease Primers*, vol. 7, 1 Dec. 2021.

[12] M. D. Hurd, P. Martorell, A. Delavande, K. J. Mullen, and K. M. Langa, "Monetary costs of dementia in the united states," *New England Journal of Medicine*, vol. 368, pp. 1326–1334, 14 Apr. 2013.

[13] Z. Breijyeh and R. Karaman, "Comprehensive review on alzheimer's disease: Causes and treatment," *Molecules*, vol. 25, no. 24, p. 5789, 2020.

[14] A. Association, "2023 alzheimer's disease facts and figures," *Alzheimer's & Dementia*, vol. 19, no. 4, pp. 1598–1695, 2023.

[15] L. Drew and M. Ashour, "An age-old story," *Age*, vol. 2050, p. 2050, 2015.

[16] E. D. Roberson and L. Mucke, "100 years and counting: Prospects for defeating alzheimer's disease," *science*, vol. 314, no. 5800, pp. 781–784, 2006.

[17] L. Mucke, "Alzheimer's disease," *Nature*, vol. 461, no. 7266, pp. 895–897, 2009.

[18] R. S. Madnani, "Alzheimer's disease: A mini-review for the clinician," *Frontiers in Neurology*, vol. 14, 2023.

[19] M. B. Abubakar *et al.*, "Alzheimer's disease: An update and insights into pathophysiology," *Frontiers in Aging Neuroscience*, vol. 14, Mar. 2022.

[20] D. Xia *et al.*, "Novel app knock-in mouse model shows key features of amyloid pathology and reveals profound metabolic dysregulation of microglia," *Molecular Neurodegeneration*, vol. 17, 1 Dec. 2022.

[21] A. Serrano-Pozo, S. Das, and B. T. Hyman, "Apoe and alzheimer's disease: Advances in genetics, pathophysiology, and therapeutic approaches," *The Lancet Neurology*, vol. 20, pp. 68–80, 1 2021.

[22] K. G. Yiannopoulou and S. G. Papageorgiou, "Current and future treatments in alzheimer disease: An update," *Journal of Central Nervous System Disease*, vol. 12, 2020.

[23] J. Weller and A. Budson, "Current understanding of alzheimer's disease diagnosis and treatment," *F1000Research*, vol. 7, 2018.

[24] M. A. Deture and D. W. Dickson, "The neuropathological diagnosis of alzheimer's disease," *Molecular Neurodegeneration*, vol. 14, 1 Aug. 2019.

[25] V. Mantzavinos and A. Alexiou, "Biomarkers for alzheimer's disease diagnosis," *Current Alzheimer Research*, vol. 14, 11 Feb. 2017.

[26] J. Rasmussen and H. Langerman, "Alzheimer's disease – why we need early diagnosis," *Degenerative Neurological and Neuromuscular Disease*, vol. Volume 9, pp. 123–130, Dec. 2019.

[27] L. Chu, "Alzheimer's disease: Early diagnosis and treatment," 2012.

[28] M. Z. Zhong, T. Peng, M. L. Duarte, M. Wang, and D. Cai, "Updates on mouse models of alzheimer's disease," *Molecular Neurodegeneration*, vol. 19, 1 Dec. 2024.

[29] C. Ma, F. Hong, and S. Yang, "Amyloidosis in alzheimer's disease: Pathogeny, etiology, and related therapeutic directions," *Molecules*, vol. 27, 4 Feb. 2022.

[30] H. Hampel *et al.*, "The amyloid-beta pathway in alzheimer's disease," *Molecular Psychiatry*, vol. 26, pp. 5481–5503, 10 Oct. 2021.

[31] R. Medeiros, D. Baglietto-Vargas, and F. M. Laferla, "The role of tau in alzheimer's disease and related disorders," *CNS Neuroscience and Therapeutics*, vol. 17, pp. 514–524, 5 Oct. 2011.

[32] C. K. Kim, Y. R. Lee, L. Ong, M. Gold, A. Kalali, and J. Sarkar, "Alzheimer's disease: Key insights from two decades of clinical trial failures," *Journal of Alzheimer's Disease*, vol. 87, pp. 83–100, 1 2022.

[33] Y. Xu, M. Zhao, Y. Han, and H. Zhang, "Gabaergic inhibitory interneuron deficits in alzheimer's disease: Implications for treatment," *Frontiers in Neuroscience*, vol. 14, Jun. 2020.

[34] M. A. Busche *et al.*, "Clusters of hyperactive neurons near amyloid plaques in a mouse model of alzheimer's disease," *Science*, vol. 321, no. 5896, pp. 1686–1689, 2008.

[35] K. E. Davis, S. Fox, and J. Gigg, "Increased hippocampal excitability in the 3xtgad mouse model for alzheimer's disease in vivo," *PLOS ONE*, vol. 9, no. 1, e91203, 2014.

[36] M. A. Busche and A. Konnerth, "Neuronal hyperactivity–a key defect in alzheimer's disease?" *Bioessays*, vol. 37, pp. 624–632, 2015.

[37] M. Shimojo *et al.*, "Selective disruption of inhibitory synapses leading to neuronal hyperexcitability at an early stage of tau pathogenesis in a mouse model," *Journal of Neuroscience*, vol. 40, pp. 3491–3501, 2020.

[38] T. Nuriel *et al.*, "Neuronal hyperactivity due to loss of inhibitory tone in apoe4 mice lacking alzheimer's disease-like pathology," *Nature Communications*, vol. 8, p. 1464, 2017.

[39] L. Lamoureux, F. M. Marottoli, K. Y. Tseng, and L. M. Tai, "Apoe4 promotes tonic-clonic seizures, an effect modified by familial alzheimer's disease mutations," *Frontiers in Cell and Developmental Biology*, vol. 9, p. 576, 2021.

[40] R. Minkeviciene *et al.*, "Amyloid beta-induced neuronal hyperexcitability triggers progressive epilepsy," *Journal of Neuroscience*, vol. 29, pp. 3453–3462, 2009.

[41] M. A. Busche *et al.*, "Decreased amyloid-beta and increased neuronal hyperactivity by immunotherapy in alzheimer's models," *Nature Neuroscience*, vol. 18, pp. 1725–1727, 2015.

[42] Y. Bai *et al.*, "Abnormal dendritic calcium activity and synaptic depotentiation occur early in a mouse model of alzheimer's disease," *Molecular Neurodegeneration*, vol. 12, pp. 1–15, 2017.

[43] E. C. B. Johnson *et al.*, "Behavioral and neural network abnormalities in human app transgenic mice resemble those of app knock-in mice and are modulated by familial alzheimer's disease mutations but not by inhibition of bace1," *Molecular Neurodegeneration*, vol. 15, pp. 1–26, 2020.

[44] V. J. Olah, A. M. Goettemoeller, J. Dimidschstein, and M. J. Rowan, "Biophysical kv channel alterations dampen excitability of cortical pv interneurons and contribute to network hyperexcitability in early alzheimer's," *eLife*, vol. 2021.10.25.465789, 2021.

[45] J. J. Palop and L. Mucke, "Network abnormalities and interneuron dysfunction in alzheimer disease," *Nature Reviews Neuroscience*, vol. 17, pp. 777–792, 2016.

[46] M. Shimojo *et al.*, "Selective disruption of inhibitory synapses leading to neuronal hyperexcitability at an early stage of tau pathogenesis in a mouse model," *Journal of Neuroscience*, vol. 40, pp. 3491–3501, 2020.

[47] S. Ghatak *et al.*, "Mechanisms of hyperexcitability in alzheimer's disease hipsc-derived neurons and cerebral organoids vs isogenic controls," *eLife*, vol. 8, e50333, 2019.

[48] S. Zhou and Y. Yu, "Synaptic e-i balance underlies efficient neural coding," *Frontiers in Neuroscience*, vol. 12, p. 46, 2018.

[49] B. R. Ferguson and W. J. Gao, "Pv interneurons: Critical regulators of e/i balance for prefrontal cortex-dependent behavior and psychiatric disorders," *Frontiers in Neural Circuits*, vol. 12, May 2018.

[50] L. Nahar, B. M. Delacroix, and H. W. Nam, "The role of parvalbumin interneurons in neurotransmitter balance and neurological disease," *Frontiers in Psychiatry*, vol. 12, 2021.

[51] L. E. Arroyo-Garcia *et al.*, "Impaired spike-gamma coupling of area ca3 fast-spiking interneurons as the earliest functional impairment in the appnl-g-f mouse model of alzheimer's disease," *Molecular Psychiatry*, pp. 1–11, 2021.

[52] T. Nuriel *et al.*, "Neuronal hyperactivity due to loss of inhibitory tone in apoe4 mice lacking alzheimer's disease-like pathology," *Nature Communications*, vol. 8, p. 1464, 2017.

[53] Y. Li *et al.*, "Reversible gabaergic dysfunction involved in hippocampal hyperactivity predicts early-stage alzheimer disease in a mouse model," *Alzheimer's Research & Therapy*, vol. 13, p. 114, 2021.

[54] P. B. Sederberg *et al.*, "Hippocampal and neocortical gamma oscillations predict memory formation in humans," *Cerebral Cortex*, vol. 17, pp. 1190–1196, 2007.

[55] A. Caccavano *et al.*, "Inhibitory parvalbumin basket cell activity is selectively reduced during hippocampal sharp wave ripples in a mouse model of familial alzheimer's disease," *Journal of Neuroscience*, vol. 40, pp. 5116–5136, 2020.

[56] L. Chen, T. Saito, T. C. Saido, and I. Mody, "Novel quantitative analyses of spontaneous synaptic events in cortical pyramidal cells reveal subtle parvalbumin-expressing interneuron dysfunction in a knock-in mouse model of alzheimer's disease," *eNeuro*, vol. 5, ENEURO.0059–18.2018, 2018.

[57] M. Martinez-Losa *et al.*, "Nav1.1-overexpressing interneuron transplants restore brain rhythms and cognition in a mouse model of alzheimer's disease," *Neuron*, vol. 0, 2018.

[58] A. L. Petrache *et al.*, "Aberrant excitatory–inhibitory synaptic mechanisms in entorhinal cortex microcircuits during the pathogenesis of alzheimer's disease," *Cerebral Cortex*, vol. 29, pp. 1834–1850, 2019.

[59] L. Verret *et al.*, "Inhibitory interneuron deficit links altered network activity and cognitive dysfunction in alzheimer model," *Cell*, vol. 149, pp. 708–721, 2012.

[60] F. Kamenetz *et al.*, "App processing and synaptic function," *Neuron*, vol. 37, pp. 925–937, 2003.

[61] J. R. Cirrito *et al.*, "Synaptic activity regulates interstitial fluid amyloid-beta levels in vivo," *Neuron*, vol. 48, pp. 913–922, 2005.

[62] K. Yamamoto *et al.*, "Chronic optogenetic activation augments abeta pathology in a mouse model of alzheimer disease," *Cell Reports*, vol. 11, pp. 859–865, 2015.

[63] B. G. Kornreich, "The patch clamp technique: Principles and technical considerations," *Journal of Veterinary Cardiology*, vol. 9, no. 1, pp. 25–37, May 2007.

[64] S. Grosser, F. J. Barreda, P. Beed, D. Schmitz, S. A. Booker, and I. Vida, "Parvalbumin Interneurons Are Differentially Connected to Principal Cells in Inhibitory Feedback Microcircuits along the Dorsoventral Axis of the Medial Entorhinal Cortex," *eneuro*, vol. 8, no. 1, pp. 0354–20, Jan. 2021.

[65] L. E. Linders *et al.*, "Studying Synaptic Connectivity and Strength with Optogenetics and Patch-Clamp Electrophysiology," vol. 23, no. 19, 2022.

[66] G. Qi, G. Radnikow, and D. Feldmeyer, "Electrophysiological and morphological characterization of neuronal microcircuits in acute brain slices using paired patch-clamp recordings.," *Journal of visualized experiments: JoVE*, no. 95, p. 52 358, Jan. 2015.

[67] R. E. Perszyk *et al.*, "Automated Intracellular Pharmacological Electrophysiology for Ligand-Gated Ionotropic Receptor and Pharmacology Screening," *Molecular Pharmacology*, vol. 100, no. 1, 73 LP –82, Jul. 2021.

[68] S. A. Kodirov, "Whole-cell patch-clamp recording and parameters," *Biophysical Reviews*, vol. 15, pp. 257–288, 2023.

[69] S. Ahmadi *et al.*, "From squid giant axon to automated patch-clamp: Electrophysiology in venom and antivenom research," *Frontiers in Pharmacology*, vol. 14, 2023.

[70] L. A. Annecchino and S. R. Schultz, "Progress in automating patch clamp cellular physiology," *Brain Neuroscience Advances*, vol. 2, 2018.

[71] C. F. Lewallen *et al.*, "High-yield, automated intracellular electrophysiology in retinal pigment epithelia," *Journal of Neuroscience Methods*, vol. 328, no. April, p. 108 442, 2019.

[72] I. Kolb *et al.*, "PatcherBot: a single-cell electrophysiology robot for adherent cells and brain slices," *Journal of Neural Engineering*, vol. 16, no. 4, p. 046 003, Aug. 2019.

[73] Q. Wu *et al.*, "Integration of autopatching with automated pipette and cell detection in vitro," *Journal of Neurophysiology*, vol. 116, no. 4, pp. 1564–1578, 2016.

[74] G. L. Holst *et al.*, "Autonomous patch-clamp robot for functional characterization of neurons in vivo: Development and application to mouse visual cortex," *Journal of Neurophysiology*, vol. 121, no. 6, pp. 2341–2357, 2019.

[75] H. J. Suk, I. van Welie, S. B. Kodandaramaiah, B. Allen, C. R. Forest, and E. S. Boyden, "Closed-Loop Real-Time Imaging Enables Fully Automated Cell-Targeted Patch-Clamp Neural Recording In Vivo," *Neuron*, vol. 95, no. 5, 1037–1047.e11, 2017.

[76] L. A. Annecchino, A. R. Morris, C. S. Copeland, O. E. Agabi, P. Chadderton, and S. R. Schultz, "Robotic Automation of In Vivo Two-Photon Targeted Whole-Cell Patch-Clamp Electrophysiology," *Neuron*, vol. 95, no. 5, 1048–1055.e3, 2017.

[77] W. A. Stoy *et al.*, "Robotic navigation to subcortical neural tissue for intracellular electrophysiology in vivo," *Journal of Neurophysiology*, vol. 118, no. 2, pp. 1141–1150, 2017.

[78] I. Kolb *et al.*, "Automated, in-vivo, whole-cell electrophysiology using an integrated patch-clamp amplifier," *BMC Neuroscience*, vol. 14, no. Suppl 1, P131, 2013.

[79] Kodandaramaiah, S. B., G. T. Franzesi, B. Y. Chow, E. S. Boyden, and C. R. Forest, "Automated whole-cell patch-clamp electrophysiology in vivo," *Nature Methods*, vol. 9, pp. 585–587, 2012.

[80] K. Koos *et al.*, "Automatic deep learning driven label-free image guided patch clamp system for human and rodent in vitro slice physiology," *nature communications*, 2021.

[81] K. Koos, J. Molnar, and P. Horvath, "Pipette Hunter: Patch-Clamp Pipette Detection," *Lecture Notes in Computer Science (including subseries Lecture Notes in Artificial Intelligence and Lecture Notes in Bioinformatics)*, vol. 10270 LNCS, p. V, 2017.

[82] B. Long, L. Li, U. Knoblich, H. Zeng, and H. Peng, "3D Image-Guided Automatic Pipette Positioning for Single Cell Experiments in vivo," *Scientific Reports*, vol. 5, no. July, pp. 1–8, 2015.

[83] J. Lee, I. Kolb, C. R. Forest, and C. J. Rozell, "Cell Membrane Tracking in Living Brain Tissue Using Differential Interference Contrast Microscopy," *IEEE Transactions on Image Processing*, vol. 27, no. 4, pp. 1847–1861, Apr. 2018.

[84] L. Z. Fan *et al.*, "All-Optical Electrophysiology Reveals the Role of Lateral Inhibition in Sensory Processing in Cortical Layer 1," vol. 180, no. 3, 521–535.e18, 2020.

[85] E. Kiskinis *et al.*, "All-Optical Electrophysiology for High-Throughput Functional Characterization of a Human iPSC-Derived Motor Neuron Model of ALS," vol. 10, no. 6, pp. 1991–2004, 2018.

[86] D. R. Hochbaum *et al.*, "All-optical electrophysiology in mammalian neurons using engineered microbial rhodopsins," *Nature Methods*, vol. 11, no. 8, pp. 825–833, 2014.

[87] Y. Adam *et al.*, "Voltage imaging and optogenetics reveal behaviour-dependent changes in hippocampal dynamics," *Nature*, vol. 569, no. 7756, pp. 413–417, 2019.

[88] R. C. Gonzalez and R. E. Woods, *Digital Image Processing*, 4th ed. Pearson Education Limited, 2018, ISBN: 9780133356724.

[89] K. Zhang, M. Sun, T. X. Han, X. Yuan, L. Guo, and T. Liu, "Residual Networks of Residual Networks: Multilevel Residual Networks," *IEEE Transactions on Circuits and Systems for Video Technology*, vol. 28, no. 6, pp. 1303–1314, 2018. arXiv: 1608.02908.

[90] S. Lathuiliere, P. Mesejo, X. Alameda-Pineda, and R. Horaud, "A Comprehensive Analysis of Deep Regression," *IEEE Transactions on Pattern Analysis and Machine Intelligence*, vol. 42, no. 9, pp. 2065–2081, 2020. arXiv: 1803.08450.

[91] S. Vani and T. V. M. Rao, "An experimental approach towards the performance assessment of various optimizers on convolutional neural network," *Proceedings of the International Conference on Trends in Electronics and Informatics, ICOEI 2019*, no. Icoei, pp. 331–336, 2019.

[92] I. Goodfellow, Y. Bengio, and A. Courville, *Deep Learning*. MIT Press, 2016, http://www.deeplearningbook.org.

[93] Y. Bengio, "Practical recommendations for gradient-based training of deep architectures," *Lecture Notes in Computer Science (including subseries Lecture Notes in Artificial Intelligence and Lecture Notes in Bioinformatics)*, vol. 7700 LECTURE NO, pp. 437–478, 2012. arXiv: 1206.5533.

[94] I. The MathWorks, *Deep learning toolbox*, Natick, Massachusetts, United State, 2020.

[95] I. Kolb, W. A. Stoy, E. B. Rousseau, O. A. Moody, A. Jenkins, and C. R. Forest, "Cleaning patch-clamp pipettes for immediate reuse," *Scientific Reports*, vol. 6, pp. 1–10, 2016.

[96] C. Landry, M. Yip, I. Kolb, W. A. Stoy, M. M. Gonzalez, and C. R. Forest, "Method for rapid enzymatic cleaning for reuse of patch clamp pipettes," *Bio-Protocol*, 2020.

[97] R. B. D'Agostino, *An omnibus test of normality for moderate and large sample size*, 1971.

[98] R. B. D'Agostino and E. Pearson, "Tests for departure from normality," *Biomatrika*, vol. 60, pp. 613–622, 1971.

[99] M. Yip, M. Gonzalez, C. Valenta, M. Rowan, and C. Forest, "Deep learning-based real-time detection of neurons in brain slices for in vitro physiology," *Scientific Reports*, vol. 10270 LNCS, p. V, 2020.

[100] J. Lee, I. Kolb, C. R. Forest, and C. J. Rozell, "Cell membrane tracking in living brain tissue using differential interference contrast microscopy," *IEEE Transactions on Image Processing*, vol. 27, no. 4, pp. 1847–1861, 2018.

[101] I. Kolb *et al.*, "Patcherbot: A single-cell electrophysiology robot for adherent cells and brain slices," *Journal of Neural Engineering*, vol. 16, no. 4, pp. 1847–1861, 2019.

[102] W. Stoy *et al.*, "Robotic navigation to sub-cortical neural tissue for intracellular electrophysiology in vivo," *Journal of Neurophysiology*, vol. 118, no. 2, pp. 1141–1150, 2017.

[103] J. Redmon and A. Farhadi, "YOLOv3: An Incremental Improvement," *arXiv e-prints*, arXiv:1804.02767, arXiv:1804.02767, Apr. 2018. arXiv: 1804.02767 [cs.CV].

[104] J. Redmon, S. K. Divvala, R. B. Girshick, and A. Farhadi, "You only look once: Unified, real-time object detection," *CoRR*, vol. abs/1506.02640, 2015. arXiv: 1506.02640.

[105] R. C. Gonzalez and R. E. Woods, "Digital image processing (3rd edition)," 2006.

[106] G. Wang *et al.*, "An optogenetics- and imaging-assisted simultaneous multiple patch-clamp recording system for decoding complex neural circuits," *Nature Protocols*, vol. 10, no. 3, pp. 397–412, 2015.

[107] Y. Peng, F. X. Mittermaier, H. Planert, U. C. Schneider, H. Alle, and J. R. Geiger, "High-throughput microcircuit analysis of individual human brains through next-generation multineuron patch-clamp," *eLife*, vol. 8, Nov. 2019.

[108] R. Perin and H. Markram, "A Computer-assisted Multi-electrode Patch-clamp System," *JoVE (Journal of Visualized Experiments)*, vol. 80, no. 80, e50630, Oct. 2013.

[109] A. J. King *et al.*, "Multi-neuron intracellular recording in vivo via interacting autopatching robots," *eLife*, 2018.

[110] L. Campagnola *et al.*, "Local connectivity and synaptic dynamics in mouse and human neocortex," *Science*, vol. 375, no. 6585, eabj5861, Mar. 2023.

[111] R. Perin, T. K. Berger, and H. Markram, "A synaptic organizing principle for cortical neuronal groups," *Proceedings of the National Academy of Sciences of the United States of America*, vol. 108, no. 13, pp. 5419–5424, 2011.

[112] G. I. Vera Gonzalez, P. O. Kgwarae, and S. R. Schultz, "Two-Photon Targeted, Quad Whole-Cell Patch-Clamping Robot," *bioRxiv*, p. 2022.11.14.516499, Jan. 2023.

[113] K. P. Kepp, "Ten challenges of the amyloid hypothesis of alzheimer's disease," *Journal of Alzheimer's Disease*, vol. 55, no. 2, pp. 447–457, 2017.

[114] V. Cubinkova *et al.*, "Alternative hypotheses related to alzheimer's disease," *Bratislavske Lekarske Listy*, vol. 119, no. 4, pp. 210–216, 2018.

[115] K. A. Celone *et al.*, "Alterations in memory networks in mild cognitive impairment and alzheimer's disease: An independent component analysis," *Journal of Neuroscience*, vol. 26, no. 40, pp. 10 222–10 231, 2006.

[116] A. Hämäläinen *et al.*, "Increased fmri responses during encoding in mild cognitive impairment," *Neurobiology of aging*, vol. 28, no. 12, pp. 1889–1903, 2007.

[117] S. Y. Bookheimer *et al.*, "Patterns of brain activation in people at risk for alzheimer's disease," *New England journal of medicine*, vol. 343, no. 7, pp. 450–456, 2000.

[118] B. Dickerson *et al.*, "Increased hippocampal activation in mild cognitive impairment compared to normal aging and ad," *Neurology*, vol. 65, no. 3, pp. 404–411, 2005.

[119] S. S. Bassett *et al.*, "Familial risk for alzheimer's disease alters fmri activation patterns," *Brain*, vol. 129, no. 5, pp. 1229–1239, 2006.

[120] J. L. Jankowsky and H. Zheng, "Practical considerations for choosing a mouse model of alzheimer's disease," *Molecular neurodegeneration*, vol. 12, pp. 1–22, 2017.

[121] J. Götz, L.-G. Bodea, and M. Goedert, "Rodent models for alzheimer disease," *Nature Reviews Neuroscience*, vol. 19, no. 10, pp. 583–598, 2018.

[122] A. Myers and P. McGonigle, "Overview of transgenic mouse models for alzheimer's disease," *Current protocols in neuroscience*, vol. 89, no. 1, e81, 2019.

[123] H. Braak and E. Braak, "Neuropathological stageing of alzheimer-related changes," *Acta neuropathologica*, vol. 82, no. 4, pp. 239–259, 1991.

[124] I. Granic, M. F. Masman, P. G. Luiten, and U. L. Eisel, "Braak staging in mouse models of alzheimer's disease," *The American journal of pathology*, vol. 177, no. 4, pp. 1603–1605, 2010.

[125] K. M. Igarashi, "Entorhinal cortex dysfunction in alzheimer's disease," *Trends in Neurosciences*, vol. 46, no. 2, pp. 124–136, Feb. 2023, Epub 2022 Dec 10.

[126] T. Gómez-Isla and et al., "Profound loss of layer ii entorhinal cortex neurons occurs in very mild alzheimer's disease," *The Journal of Neuroscience*, vol. 16, no. 14, pp. 4491–4500, 1996.

[127] U. A. Khan and et al., "Molecular drivers and cortical spread of lateral entorhinal cortex dysfunction in preclinical alzheimer's disease," *Nature Neuroscience*, vol. 17, no. 3, pp. 304–311, 2014.

[128] L. Chen *et al.*, "Progressive excitability changes in the medial entorhinal cortex in the 3xtg mouse model of alzheimer's disease pathology," *bioRxiv*, p. 2023.05.30.542838, May 2023, Preprint.

[129] A. M. Goettemoeller *et al.*, "Entorhinal cortex vulnerability to human app expression promotes hyperexcitability and tau pathology," *bioRxiv*, 2023.

[130] P. G. Anastasiades and A. G. Carter, "Circuit organization of the rodent medial prefrontal cortex," *Trends in Neurosciences*, vol. 44, no. 7, pp. 550–563, Jul. 2021, Epub 2021 May 7.

[131] P. Xu, A. Chen, Y. Li, X. Xing, and H. Lu, "Medial prefrontal cortex in neurological diseases," *Physiological genomics*, vol. 51, no. 9, pp. 432–442, 2019.

[132] N. Choudhury, L. Chen, L. Al-Harthi, and X.-T. Hu, "Hyperactivity of medial prefrontal cortex pyramidal neurons occurs in a mouse model of early-stage alzheimer's disease without beta-amyloid accumulation," *Frontiers in Pharmacology*, vol. 14, 2023.

[133] Z. Zhang *et al.*, "Hyper-excitability of corticothalamic pt neurons in mpfc promotes irritability in the mouse model of alzheimer's disease," *Cell Reports*, vol. 41, 5 Nov. 2022.

[134] Y. Gu *et al.*, "Balanced activity between kv3 and nav channels determines fast-spiking in mammalian central neurons," *iScience*, vol. 9, pp. 120–137, Nov. 2018.

[135] S. J. Mitchell and R. A. Silver, "Shunting inhibition modulates neuronal gain during synaptic excitation," *Neuron*, vol. 38, no. 3, pp. 433–445, 2003.

[136] J. C. Magee, "Dendritic integration of excitatory synaptic input," *Nature Reviews Neuroscience*, vol. 1, no. 3, pp. 181–190, 2000.

[137] L. Melgosa-Ecenarro, N. Doostdar, C. I. Radulescu, J. S. Jackson, and S. J. Barnes, "Pinpointing the locus of gabaergic vulnerability in alzheimer's disease," in *Seminars in cell & developmental biology*, Elsevier, vol. 139, 2023, pp. 35–54.

[138] S. Hijazi *et al.*, "Early restoration of parvalbumin interneuron activity prevents memory loss and network hyperexcitability in a mouse model of alzheimer's disease," *Molecular Psychiatry*, vol. 25, no. 12, pp. 3380–3398, 2020.

[139] M. E. Ragozzino, S. Adams, and R. P. Kesner, "Differential involvement of the dorsal anterior cingulate and prelimbic–infralimbic areas of the rodent prefrontal cortex in spatial working memory.," *Behavioral neuroscience*, vol. 112, no. 2, p. 293, 1998.

[140] P. Gisquet-Verrier and B. Delatour, "The role of the rat prelimbic/infralimbic cortex in working memory: Not involved in the short-term maintenance but in monitoring and processing functions," *Neuroscience*, vol. 141, no. 2, pp. 585–596, 2006.

[141] J. K. Seamans, S. B. Floresco, and A. G. Phillips, "Functional differences between the prelimbic and anterior cingulate regions of the rat prefrontal cortex.," *Behavioral neuroscience*, vol. 109, no. 6, p. 1063, 1995.

[142] L. Nahar *et al.*, "Regulation of pv-specific interneurons in the medial prefrontal cortex and reward-seeking behaviors," *Journal of neurochemistry*, vol. 156, no. 2, pp. 212–224, 2021.

[143] A. N. Binette *et al.*, "Parvalbumin-positive interneurons in the medial prefrontal cortex regulate stress-induced fear extinction impairments in male and female rats," *Journal of Neuroscience*, vol. 43, no. 22, pp. 4162–4173, 2023.

[144] S. Shu *et al.*, "Prefrontal parvalbumin interneurons deficits mediate early emotional dysfunction in alzheimer's disease," *Neuropsychopharmacology*, vol. 48, no. 2, pp. 391–401, 2023.

[145] S. Liebscher, G. B. Keller, P. M. Goltstein, T. Bonhoeffer, and M. Hübener, "Selective persistence of sensorimotor mismatch signals in visual cortex of behaving alzheimer's disease mice," *Current Biology*, vol. 26, no. 7, pp. 956–964, 2016.

[146] J. Liepert, K. Bär, U. Meske, and C. Weiller, "Motor cortex disinhibition in alzheimer's disease," *Clinical Neurophysiology*, vol. 112, no. 8, pp. 1436–1441, 2001.

[147] F. Ferreri, F. Pauri, P. Pasqualetti, R. Fini, G. Dal Forno, and P. M. Rossini, "Motor cortex excitability in alzheimer's disease: A transcranial magnetic stimulation

study," *Annals of Neurology: Official Journal of the American Neurological Association and the Child Neurology Society*, vol. 53, no. 1, pp. 102–108, 2003.

[148] E. Khedr, M. Ahmed, E. Darwish, and A. Ali, "The relationship between motor cortex excitability and severity of alzheimer's disease: A transcranial magnetic stimulation study," *Neurophysiologie Clinique/Clinical Neurophysiology*, vol. 41, no. 3, pp. 107–113, 2011.

[149] E. Orta-Salazar, A. Feria-Velasco, and S. Díaz-Cintra, "Primary motor cortex alterations in alzheimer disease: A study in the 3xtg-ad model," *Neurología (English Edition)*, vol. 34, no. 7, pp. 429–436, 2019.